CELL BIOLOGY

Decoding the interplay between m^{6}A modification and stress granule stability by live-cell imaging

Qianqian Li[1], Jian Liu[1], Liping Guo[1,2], Yi Zhang[1], Yanwei Chen[1,3], Huijuan Liu[1,4], Hongyu Cheng[5], Lin Deng[1], Juhui Qiu[5], Ke Zhang[1], Wee Siong Sho Goh[1], Yingxiao Wang[6], Qin Peng[1]*

***N*^{6}-methyladenosine (m^{6}A)–modified mRNAs and their cytoplasmic reader YTHDFs are colocalized with stress granules (SGs) under stress conditions, but the interplay between m^{6}A modification and SG stability remains unclear. Here, we presented a spatiotemporal m^{6}A imaging system (SMIS) that can monitor the m^{6}A modification and the translation of mRNAs with high specificity and sensitivity in a single live cell. SMIS showed that m^{6}A-modified reporter mRNAs dynamically enriched into SGs under arsenite stress and gradually partitioned into the cytosol as SG disassembled. SMIS revealed that knockdown of YTHDF2 contributed to SG disassembly, resulting in the fast redistribution of mRNAs from SGs and rapid recovery of stalled translation. The mechanism is that YTHDF2 can regulate SG stability through the interaction with G3BP1 in m^{6}A-modified RNA-dependent manner. Our results suggest a mechanism for the interplay between m^{6}A modification and SG through YTHDF2 regulation.**

INTRODUCTION

N^6-methyladenosine (m^{6}A) is the most abundant internal modification of various types of RNAs and regulates RNA transcription (*1*, *2*), splicing (*3*), transport (*4*), decay (*5*), and translation (*6*, *7*). The maladjustment of disease-related transcripts by m^{6}A modification has been identified as a potential target for clinical therapy (*8*–*10*). Now, there is a consensus that distinct m^{6}A reader proteins mediate their respective signaling pathways in development-dependent and tissue-specific manners (*11*, *12*). Through newly established RNA sequencing methods, studies on m^{6}A function can focus on holistic analysis of the whole transcriptome (*13*–*18*). However, the conclusions of studies have been divergent due to distinct sequencing strategies and data processing logics. It is still debatable whether the YT521-B homology (YTH) domain-containing family proteins (YTHDFs) perform unique or redundant roles in mRNA translation and stability (*19*, *20*).

Stress granules (SGs) are microscopic droplets that can result from stressors, such as heat shock, osmotic pressure, and $NaAsO_2$ treatment (*21*, *22*). SG formation is accompanied by a global inhibition of translation and enrichment of mRNAs and RNA binding proteins in SGs (*23*–*25*). Recently, researchers reported that m^{6}A-modified mRNAs and YTHDFs are located in SGs (*26*–*28*). The interaction of YTHDFs with multivalent m^{6}A-modified RNAs promotes the liquid-liquid phase separation (LLPS) (*27*, *29*, *30*). Knockdown of YTHDF1/3 impairs the formation of SG (*28*). However, the function of m^{6}A modification in promoting the enrichment of mRNAs in SGs remains debatable, and the role of m^{6}A readers in SG disassembly has not been explored (*31*). Therefore, spatiotemporally monitoring the dynamics of m^{6}A-modified RNA during SG formation and disassembly is important for clarifying how m^{6}A RNA and its readers contribute to SG stability.

Several imaging methods have been developed to detect m^{6}A-modified RNA in mammalian cells. For m^{6}A-specific in situ hybridization mediated proximity ligation assay (m^{6}AISH-PLA) (*32*) and deamination adjacent to RNA modification targets-fluorescent in situ hybridization (DART-FISH) (*33*), rolling cycle amplification was used to quantify m^{6}A modification events in situ in fixed cells. The YTH-APOBEC1 editable green fluorescent protein (GFP) reporter was used in the genetically encoded m^{6}A sensor (GEMS) system to transform the m^{6}A modification level to a fluorescent intensity and determine the global activity of m^{6}A methyltransferases (*34*). Although the GEMS system provides a real-time readout of m^{6}A levels in living cells, spatial and temporal imaging cannot be achieved because the system uses a one-shot technique for measurements. Thus, new imaging methods with high spatiotemporal resolution are urgently needed to precisely study the function and dynamics of m^{6}A-modified RNA in living cells.

In this study, we developed a spatiotemporal m^{6}A imaging system (SMIS) that contained a m^{6}A-modified reporter mRNA and fluorescence resonance energy transfer (FRET) biosensors. Using the SMIS, we demonstrated that after transcription, the reporter mRNA could recruit methyltransferase like 3 (METTL3) to methylate N^6 site of adenosine; then, the mRNA was transported out of the nucleus for translation into mMaroon1 as a fluorescent readout. Moreover, a FRET biosensor with a YTH domain and MS2 coat protein (MCP) recognizes m^{6}A modifications and adjacent MS2 loops, resulting in high FRET, which can indicate high m^{6}A levels in real time. With that system, we can dynamically monitor transcription, m^{6}A modification, and translation of reporter mRNAs in a single live cell. We showed that our reporter mRNAs in SMIS were dynamically enriched in SGs under arsenite stress, and a higher FRET signal was attained in SGs than the cytosol. In addition, we investigated the function of m^{6}A cytoplasmic readers in SG disassembly. YTHDF2 knockdown accelerated the disassembly of SGs, the redistribution of mRNAs from SGs, and the recovery of stalled translation. We elucidated the mechanism by which YTHDF2 regulated SG stability through interaction with G3BP1 in m^{6}A-modified RNA-dependent manner.

[1]Shenzhen Bay Laboratory, Shenzhen 518132, China. [2]School of Biology and Biological Engineering, South China University of Technology, Guangzhou 510006, China. [3]Department of Biology, School of Life Sciences, Southern University of Science and Technology, Shenzhen 518055, China. [4]State Key Laboratory of Crop Stress Biology for Arid Areas, College of Life Sciences, Northwest A&F University, Yangling 712100, Shaanxi, China. [5]Key Laboratory for Biorheological Science and Technology of Ministry of Education, State and Local Joint Engineering Laboratory for Vascular Implants, College of Bioengineering, Chongqing University, Chongqing 400030, China. [6]Alfred E. Mann Department of Biomedical Engineering, University of Southern California, Los Angeles, CA, USA.
*Corresponding author. Email: pengqin@szbl.ac.cn

RESULTS

In vitro FRET system monitors m^{6}A modifications dynamically

Genetically encoded FRET biosensors can transform compound levels (*35*, *36*), kinase activity (*37*, *38*), and posttranslational modifications (*39*) into images with spatiotemporal resolution. To conceptually test the feasibility of the FRET system for dynamically monitoring m^{6}A modifications in vitro, we first designed a m^{6}A-modified artificial RNA (m^{6}A aRNA) that contained the m^{6}A consensus motif GGACU and an MS2 aptamer (Fig. 1A). The fusion of MCP to enhanced cyan fluorescent protein (ECFP) formed the FRET donor protein MCP-ECFP, which bound to MS2 aptamers on m^{6}A-modified and unmodified aRNAs (fig. S1A). The fusion of the YTH domain from YTHDF2 to YPet (a variant of yellow fluorescent protein) resulted in the FRET acceptor protein YTH-YPet, which specifically recognized m^{6}A aRNA but not the unmodified version (fig. S1B).

After YTH-YPet was incubated with MCP-ECFP and m^{6}A aRNA, a marked reduction in donor emission at approximately 478 nm and an increase in acceptor emission at approximately 528 nm were observed compared to those of the control groups with the mutant YTH-YPet (YTH-YPet 3A) or unmodified aRNA (Fig. 1B). Moreover, associations among MCP-ECFP, YTH-YPet, and m^{6}A aRNAs were revealed by an electrophoretic mobility shift assay. In the control groups, only the association of MCP-ECFP with RNA was detected (Fig. 1C). These results indicated that YTH-YPet can specifically associate with m^{6}A-modified aRNAs in combination with MCP-ECFP to detect m^{6}A modifications through FRET. After m^{6}A aRNA was added to the mixture of MCP-ECFP and YTH-YPet, a rapid increase in the FRET ratio (528/478 nm) was observed. The FRET ratio gradually decreased after treatment with ribonuclease (RNase) in different concentrations, indicating that FRET signal was RNA dependent (fig. S1C). The METTL3/14 complex is the major methyltransferase involved in m^{6}A modifications of mRNAs (*40*). In the system that contained YTH-YPet, MCP-ECFP, and aRNA, the FRET ratio slowly increased upon the addition of the METTL3/14 complex and *S*-adenosylmethionine (SAM), the methyl donor for m^{6}A modification; this result revealed the kinetics of METTL3/14 complex activity (Fig. 1D). Consistent results were also found in

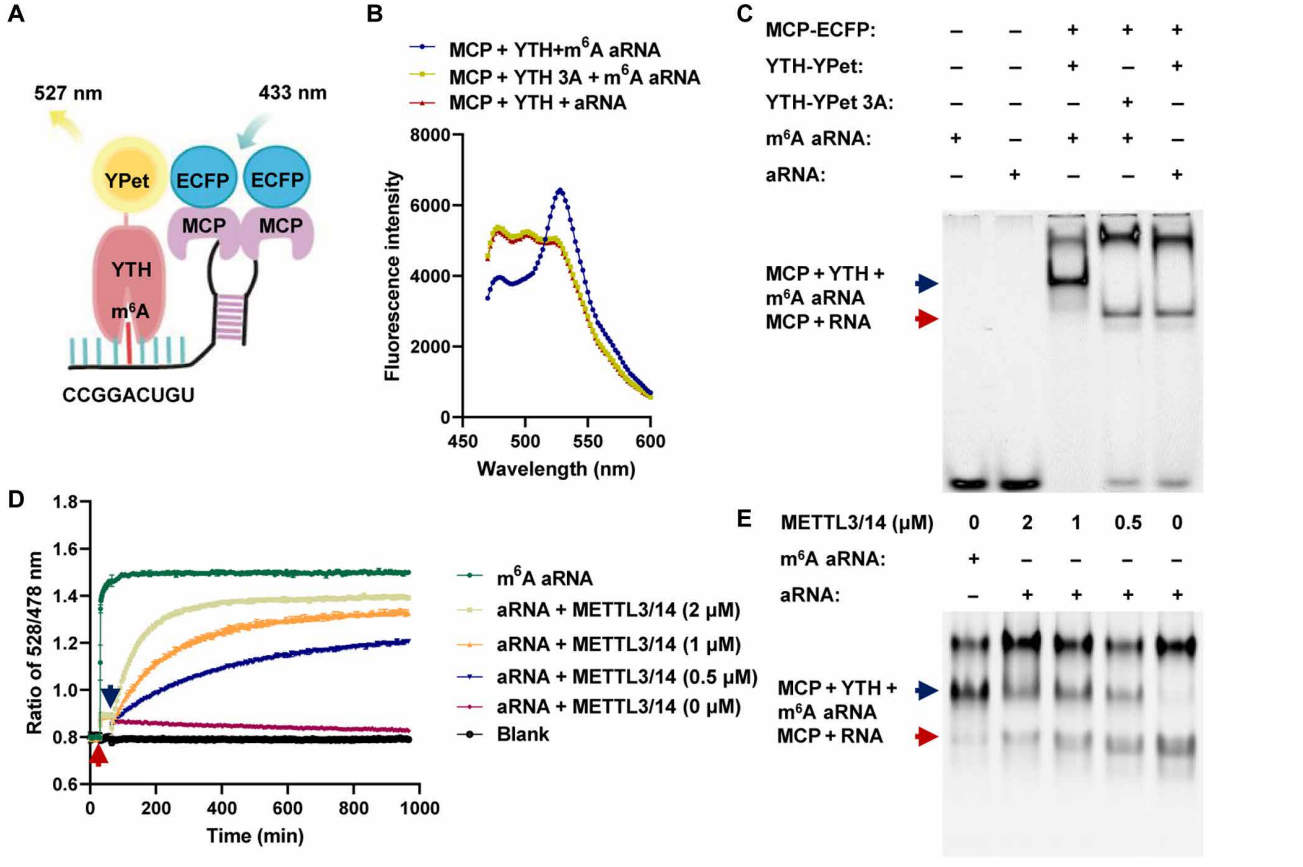

Fig. 1. In vitro FRET system for detecting m^{6}A modifications on aRNAs. (**A**) Schematic diagram of the FRET system based on m^{6}A aRNAs. (**B**) Fluorescence spectrum after MCP-ECFP, YTH-YPet, or YTH-YPet-3A was mixed with aRNA or m^{6}A aRNA. (**C**) Gel red staining of native polyacrylamide gel electrophoresis (PAGE) after MCP-ECFP, YTH-YPet, or YTH-YPet-3A was mixed with aRNA or m^{6}A aRNA; (i) m^{6}A aRNA, (ii) aRNA (iii) MCP-ECFP + YTH-YPet + m^{6}A aRNA; (iv) MCP-ECFP + YTH-YPet-3A + m^{6}A aRNA, and (v) MCP-ECFP + YTH-YPet + aRNA; blue arrow: the complex of YTH, MCP, and m^{6}A aRNA; red arrow: the complex of MCP and RNA. (**D**) Ratio of 528/478-nm emission after MCP-ECFP and YTH-YPet were mixed; the red arrow indicates the addition of aRNA or m^{6}A aRNA, and the blue arrow indicates the addition of METTL3/14 at different concentrations; $n = 3$. (**E**) Gel red staining of native PAGE for (D) (i) m^{6}A aRNA + YTH-YPet + MCP-ECFP, (ii) aRNA + YTH-YPet + MCP-ECFP + METTL3 (2 μM), (iii) aRNA + YTH-YPet + MCP-ECFP + METTL3 (1 μM), (iv) aRNA + YTH-YPet + MCP-ECFP + METTL3 (0.5 μM), (v) aRNA + YTH-YPet + MCP-ECFP + METTL3 (0 μM); the blue arrow indicates the complex of YTH, MCP, and m^{6}A aRNA; the red arrow indicates the complex of MCP and RNA.

the fluorescence spectrum, as the donor emission decreased, and the acceptor emission increased (fig. S1D). ESMA revealed the band that corresponded to the association of MCP-ECFP, YTH YPet, and m^{6}A aRNA after catalysis by the METTL3/14 complex (Fig. 1E). The change in the m^{6}A modification level after METTL3/14 complex treatment was further measured via a dot blot (fig. S1E). Together, the above results demonstrated that the in vitro FRET system we developed can monitor the dynamical m^{6}A modifications of aRNAs by the METTL3/14 complex with high sensitivity and specificity.

SMIS detects m^{6}A modifications in living cells with high spatiotemporal resolutions

To spatiotemporally track m^{6}A-modified RNA in living cells, the FRET signal must be amplified. Therefore, we designed a m^{6}A reporter plasmid that contained transcriptional regulatory elements (TREs), peroxisome signal peptide (SKL) fused to mCherry, and a 22x m^{6}A tandem motif (GGACU) linked with corresponding MS2 aptamers, followed by an independently expressed reverse tetracycline transactivator (fig. S2A). According to the in vitro design of FRET biosensors, we first coexpressed MCP-ECFP and a YTH-YPet protein that was cleaved by the P2A linker in a single cell. However, the FRET ratio did not significantly change between the wild type (WT) and mutant biosensors when HeLa cells were cotransfected with FRET biosensors and reporter mRNAs (fig. S2, B and C). Compared to intermolecular sensors, intramolecular FRET biosensors often exhibit higher sensitivity (*35*). Thus, we switched the design for m^{6}A detection in living cells to intramolecular FRET biosensors, which consist of the following parts: YTH at the N-terminus, a linker flanked by YPet and ECFP, and MCP at the C terminus (fig. S2A). The N and C termini of the biosensor bind to GGACU and adjacent MS2 on the reporter mRNA when the mRNA is methylated to generate high FRET. This integrated system, which we refer to as the SMIS, couples the FRET signal with m^{6}A modification.

To generate a SMIS with high sensitivity, we optimized the FRET biosensor by changing the linker between YPet and ECFP, the subcellular location of the fluorescence reporter, and the MCP version. We confirmed that the FRET biosensor in the YTH-YPet-EV linker ECFP-MCP format (BS-WT) exhibited a greater FRET change than that of the negative FRET biosensor with W432/486/491A mutations in YTH domain (BS-3A), which lost the specific recognition of m^{6}A modification (fig. S2, D to I). Therefore, BS-WT and BS-3A were used for the following study. Compared with BS-3A, BS-WT exhibited a greater FRET ratio in HeLa and U2OS cells after cotransfection with mCherry reporter plasmids (fig. S2, J to L), suggesting the specificity of BS-WT for monitoring the m^{6}A modifications of reporter mRNA. By replacing SKL-fused mCherry with double nuclear localization signal (NLS)–fused mMaroon1 in reporter mRNA, the FRET pairs could be separated from the reporter fluorescent protein more clearly in the spectrum and in location (Fig. 2A). A higher FRET signal was detected with the mMaroon1 reporter by BS-WT than by BS-3A after doxycycline (DOX) induction for 12 hours (Fig. 2, B to D). To demonstrate that the specificity of the FRET signal results from m^{6}A-modified reporter mRNA, we generated a control reporter mRNA with the GGTCU motif, in which the mRNA was not modified by m^{6}A. Our results showed that the FRET signal was significantly reduced in HeLa cells expressing the control reporter and BS-WT, verifying the specificity of SMIS for m^{6}A modification (Fig. 2, E to G).

To obtain relatively uniform FRET signals from SMIS, we first generated a stable HeLa cell line, i.e., the m^{6}A reporter cell line, that expressed mMaroon1 reporter genes. In the stable cell line, the puncta labeled by MCP-3×GFP were observed after DOX induction for 1 hour, which were the clusters of reporter mRNAs (Fig. 3A) and strongly colocalized with METTL3 and YTHDC1, suggesting that the reporter mRNAs can be catalyzed by endogenous METTL3 and recognized by the endogenous binder YTHDC1 (Fig. 3B). Then, on the basis of the m^{6}A reporter cell line, we delivered the FRET biosensors BS-WT and BS-3A to generate stable SMIS-WT and SMIS-3A cell lines, which functioned as WT and deficient SMIS, respectively. Compared to SMIS-WT, SMIS-3A cells contained the same m^{6}A reporter mRNA but negative FRET biosensors with W432/486/491A mutations in YTH domain (BS-3A), thus losing responsiveness to m^{6}A modification. Twelve hours after DOX induction, the mMaroon1 transcript level did not significantly differ between the SMIS-WT and SMIS-3A cell lines (Fig. 3C), whereas the FRET ratio of the SMIS-WT was significantly greater than that of the SMIS-3A cell line (Fig. 3, D and E); therefore, a stable SMIS system was successfully constructed and can detect m^{6}A modification in live cells. With METTL3 knockdown (Fig. 3F and fig. S3, A to C), the FRET ratio of SMIS-WT was notably decreased in the siMETTL3 group (Fig. 3, G and H). Compared to dimethyl sulfoxide (DMSO) treatment, the mMaroon1 intensity of SMIS-WT after STM2457 treatment, a canonical METLL3 inhibitors, had no significant change (fig. S3D), whereas the FRET ratio reduced in a concentration-dependent manner (Fig. 3, I and J, and fig. S3, E and F). Meanwhile, we quantified the relative methylation level of reporter mRNA by m6ACE sequencing methods with single base resolution according to the literature (Fig. 3, K and L, and fig. S3G) (*41*). The results indicated that the m^{6}A consensus motif in reporter RNA was extensively methylated in SMIS-WT cells, which was significantly inhibited by STM2457 treatment. In addition, the time-course FRET imaging of SMIS-WT cells after STM2457 treatment was examined. The detailed workflow was shown in fig. S3H. Specifically, SMIS-WT cells were first induced by DOX for 14 hours to achieve plateau where the FRET ratio was stable and then treated with DMSO or STM2457 and DOX, respectively (Fig. 3M). In the DMSO group, the FRET ratio remained constant after additional DOX induction for 16.5 hours. In contrast, the FRET ratio gradually decreased after STM2457 treatment, reflecting the reduction of m^{6}A reporter RNAs. The representative FRET ratio images are also shown in Fig. 3N. All the data demonstrated that SMIS could monitor the m^{6}A modification of reporter mRNA with high specificity and sensitivity.

To monitor the dynamic changes in m^{6}A modification during gene expression, we simultaneously tracked the FRET signal and mMaroon1 intensity in HeLa cells with SMIS-WT or SMIS-3A, which were expressed transiently or stably (Fig. 4, A to D). The mMaroon1 intensity gradually increased upon DOX induction in both groups. The FRET ratio in the SMIS-WT cells slowly increased and reached a plateau at 12 hours. In contrast, FRET in the SMIS-3A group remained unchanged during DOX induction, suggesting that SMIS can be used to spatiotemporally monitor m^{6}A modifications and translation of reporter mRNA for both transient expression and stable cell lines.

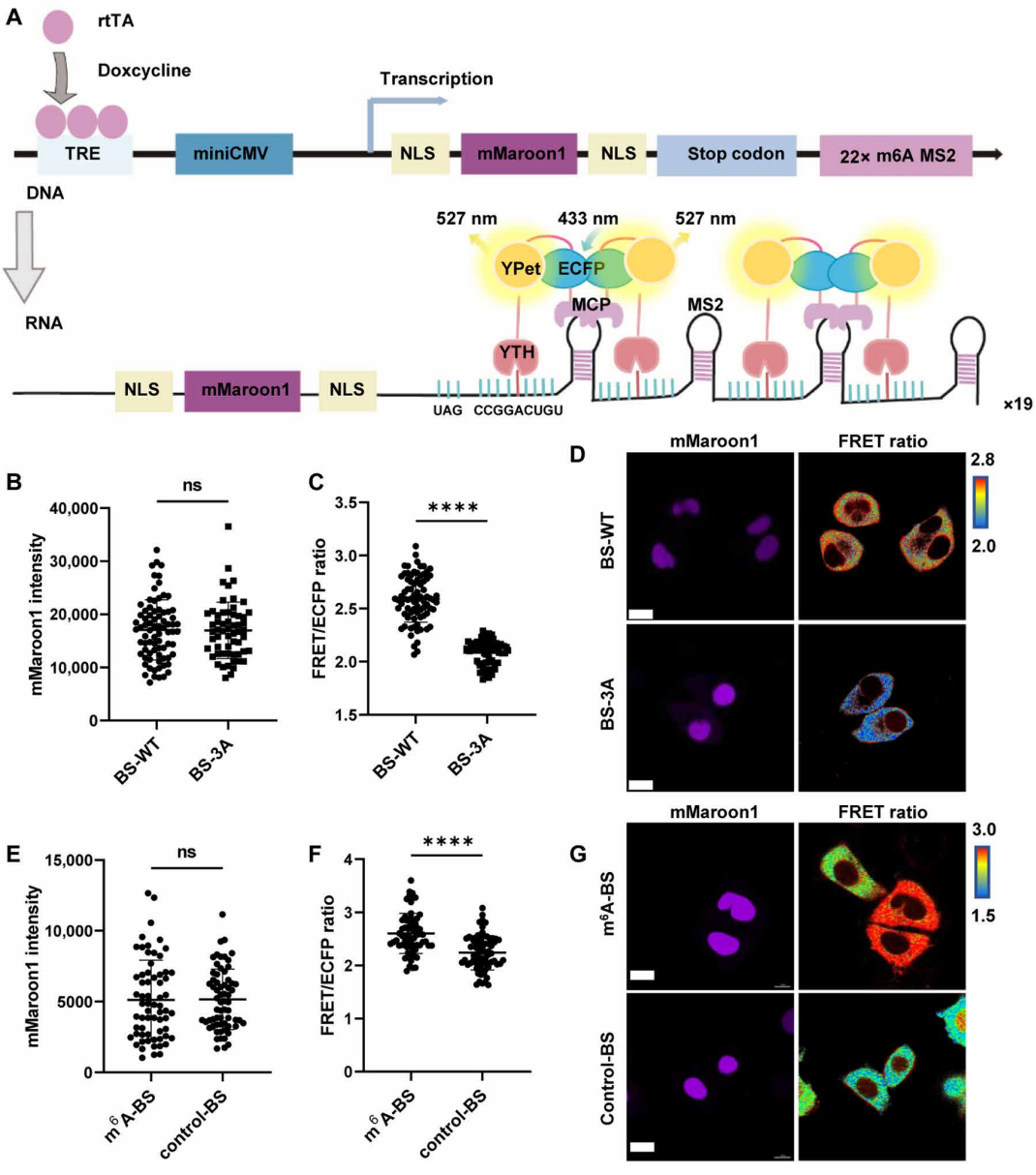

Fig. 2. Live-cell imaging of m^{6}A modifications with high specificity. (**A**) Schematic diagram of the live-cell SMIS system based on genetically encoded reporter mRNA and an intramolecular FRET biosensor. (**B**) mMaroon1 intensity in HeLa cells transiently transfected with the reporter mRNA plasmid and the BS-WT or BS-3A system for 36 hours and then subjected to DOX induction for 12 hours; unpaired *t* test with Welch's correction (BS-WT: $n = 78$; BS-3A: $n = 58$; $P = 0.927$). (**C**) Corresponding FRET/ECFP ratio from (B), unpaired *t* test with Welch's correction (BS-WT: $n = 78$; BS-3A: $n = 58$; $P < 0.0001$). (**D**) Representative images of mMaroon1 and the FRET/ECFP ratio for (B) and (C). Scale bar, 15 μm. (**E**) mMaroon1 intensity in HeLa cells transiently transfected with BS-WT and m^{6}A reporter (GGACU motif) or control reporter (GGTCU motif) for 36 hours and subjected to DOX induction for 12 hours, unpaired *t* test with Welch's correction ($n = 65$, $P = 0.9416$). (**F**) Corresponding FRET/ECFP ratio from (E), unpaired *t* test with Welch's correction ($n = 65$, $P < 0.0001$). (**G**) Representative images of mMaroon1 and the FRET/ECFP ratio for (E) and (F). Scale bar, 15 μm. ns, not significant.

SMIS monitors the dynamic enrichment of m^{6}A-modified RNA in SGs under arsenite-induced stress

SGs are organelles without membranes and are assembled through LLPS of RNA binding proteins and mRNAs under stress conditions, such as heat shock, osmotic stress (sorbitol), and oxidative stress (*42*, *43*). Recently, m^{6}A-modified mRNAs and their cytoplasmic reader proteins were reported to reside within SGs and pathological depositions, and the latter was involved in neurodegenerative diseases (*10*, *44*). However, the interplay between m^{6}A and SGs is controversial (*27*, *31*). Now, the main debates focus on the following points: Is the m^{6}A modification a deciding factor for the partitioning of mRNAs into SGs? Do m^{6}A modifications or their readers contribute to SG stability?

Using SMIS, we monitored the location and m^{6}A levels on the reporter mRNA during SG formation (Fig. 5A). The granules

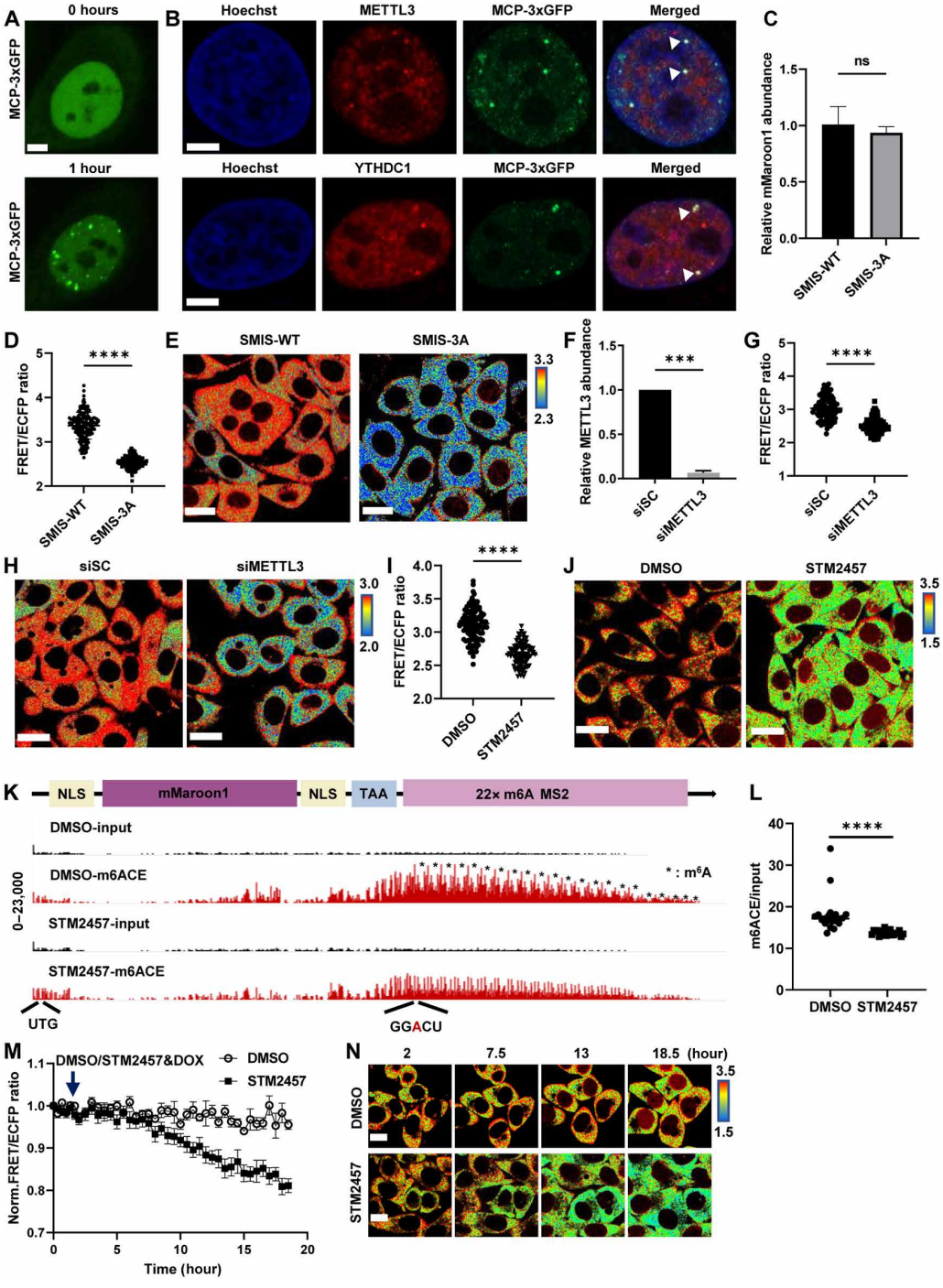

Fig. 3. SMIS detects the changes of m^{6}A modification responsive to METTL3 regulation. (**A**) MCP-3×GFP images of m^{6}A reporter cell after transient transfection with MCP-3×GFP for 36 hours and DOX induction for 1 hour. Scale bar, 5 μm. (**B**) Immunostaining for METTL3 and YTHDC1 of m^{6}A reporter cells in (A). Scale bars, 5 μm. (**C** to **E**) Relative abundance of the mMaroon1 mRNA, quantification of FRET ratio, and representative images of FRET ratio in SMIS-WT and SMIS-3A cells after DOX induction for 12 hours. Unpaired *t* test with Welch's correction [$n = 3$, $P = 0.5168$ in (C); $n = 150$, $P < 0.0001$ in (D)]. Scale bars, 20 μm. (**F**) Relative METTL3 RNA abundance in HeLa cells after siSC or siMETTL3 treatment for 48 hours. Unpaired *t* test with Welch's correction ($n = 3$, $P = 0.0002$). (**G** and **H**) Quantification of FRET ratio and representative images of FRET ratio of SMIS-WT after siSC or siMETTL3 treatment for 36 hours and DOX induction for 12 hours. Unpaired *t* test with Welch's correction ($n = 100$, $P < 0.0001$). Scale bars, 20 μm. (**I** and **J**) Quantification of FRET ratio and representative images of FRET ratio in SMIS-WT cells after pretreatment with DMSO or STM2457 for 3 hours and incubated with DMSO or STM2457 (60 μM) and DOX (1 μg/ml) for 12 hours. Unpaired *t* test with Welch's correction ($n = 100$, $P < 0.0001$). Scale bars, 20 μm. (**K**) m6ACE (red) and input (black) read-start counts [in reads per million mapped (RPM)] mapped to mMaroon1 reporter gene in (J); * means m^{6}A site on reporter mRNA. (**L**) Quantification of m6ACE/input ratio at m^{6}A site of reporter mRNA from (K). Unpaired *t* test with Welch's correction ($n = 22$, $P < 0.0001$). (**M**) Time-course FRET imaging of SMIS-WT after DMSO/STM2457 treatment, $n = 10$, specifically. (**N**) Representative FRET images in (M). Scale bars, 10 μm.

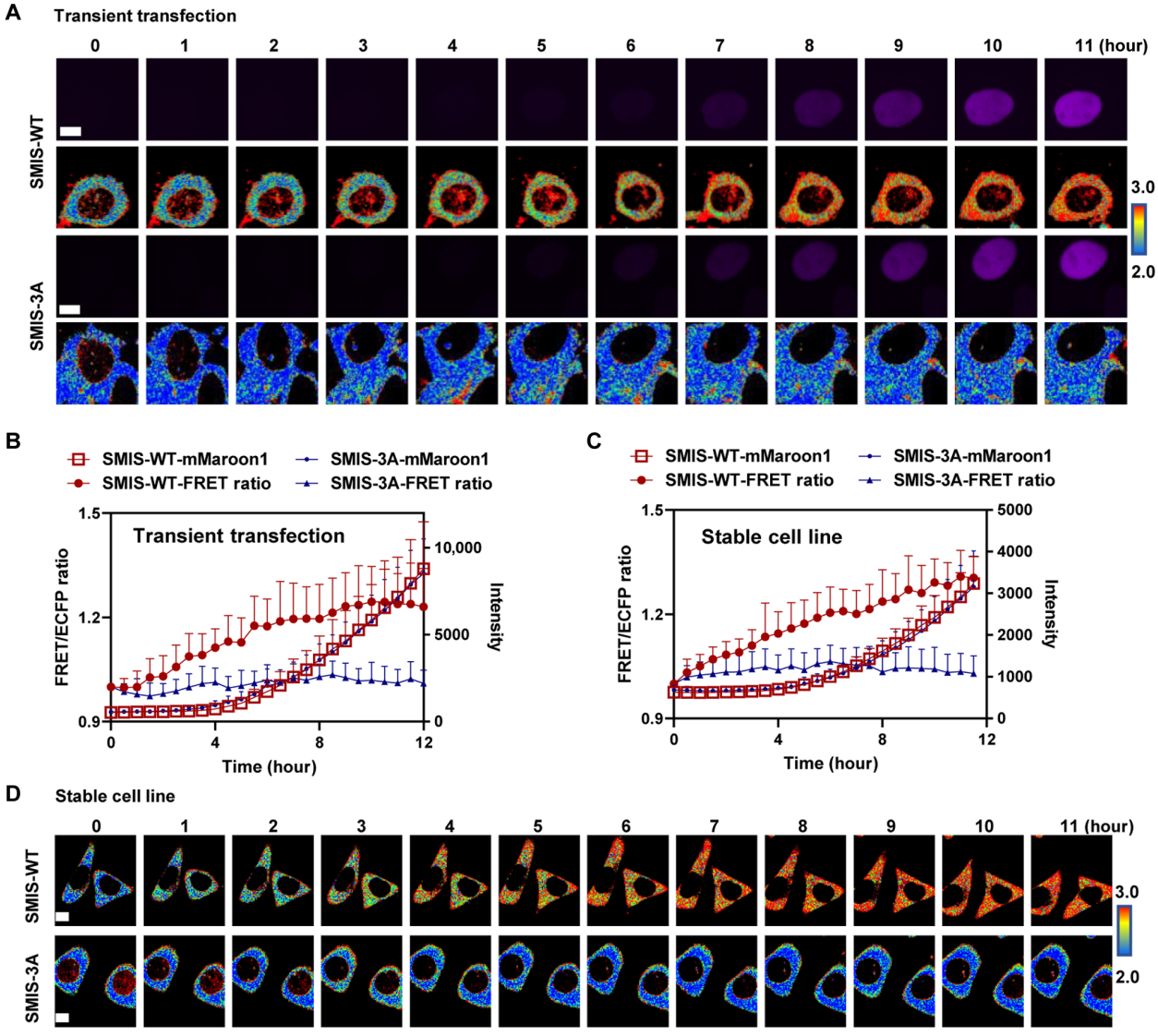

Fig. 4. SMIS detects dynamic changes in m^{6}A modifications during gene expression. (**A**) Representative time-lapse images of mMaroon1 and the FRET/ECFP ratio after transient transfection of HeLa cells with SMIS-WT or SMIS-3A for 36 hours and DOX induction over time. DOX was added at $t = 0$. Scale bars, 5 μm. (**B**) Changes in the FRET ratio and mMaroon1 intensity after transient transfection of HeLa cells with SMIS-WT or SMIS-3A for 36 hours and DOX induction. $n = 11$. (**C**) Changes in the FRET ratio and mMaroon1 intensity in the SMIS-WT and SMIS-3A stable cell lines after DOX induction. $n = 19$. (**D**) Representative time-lapse images of FRET/ECFP ratio in SMIS-WT and SMIS-3A stable cell line after DOX induction. DOX was added at $t = 0$. Scale bars, 5 μm.

formed after 20 min and matured approximately 40 to 60 min after sodium arsenite ($NaAsO_2$) treatment. After $NaAsO_2$ treatment, no matter in SMIS-WT or SMIS-3A cells, the colocalization of the SG marker G3BP1 and FRET biosensor from SMIS was identified by immunostaining (fig. S4A), indicating the localization of FRET biosensors in SGs. Then, higher FRET ratio was detected by SMIS-WT in SGs at 40 min even 1 hour than that at 0 min upon $NaAsO_2$ treatment (Fig. 5, A to C), suggesting that m^{6}A-modified reporter mRNAs preferred to locate in SG. However, there was no FRET ratio increase observed from SMIS-3A, suggesting the specificity of FRET ratio increase in SGs. SMIS-3A, as the negative control that can be m^{6}A modified but incapable of FRET, clarified that the increase of FRET ratio in SMIS-WT was not due to the aggregation of FRET biosensors in SGs but the enrichment of m^{6}A modification (Fig. 5, A to C). Putting together, our results indicated that m^{6}A-modified reporter mRNA preferred to locate in SG than in cytosol. To image the reporter mRNA at the single-molecule level, we transiently transfected the m^{6}A reporter cell line with MCP-3×GFP to label the reporter mRNAs. The results showed that most of the m^{6}A-modified reporter mRNAs colocalized with G3BP1 (Fig. 5, D and E). Single-molecule RNA FISH (smFISH) analysis of reporter mRNA by targeting the MS2 motif also revealed that most reporter mRNAs were localized in granules (fig. S4B). To further verify the location of the m^{6}A-modified RNAs, we labeled the endogenous m^{6}A-modified RNAs and their cytoplasmic reader, YTHDF2, with specific antibodies. Endogenous m^{6}A and YTHDF2 also colocalized with G3BP1 in the cytosol (Fig. 5F and fig. S4C). In addition, markedly fewer MCP-3×GFP dots was found in SGs in the siMETTL3-treated

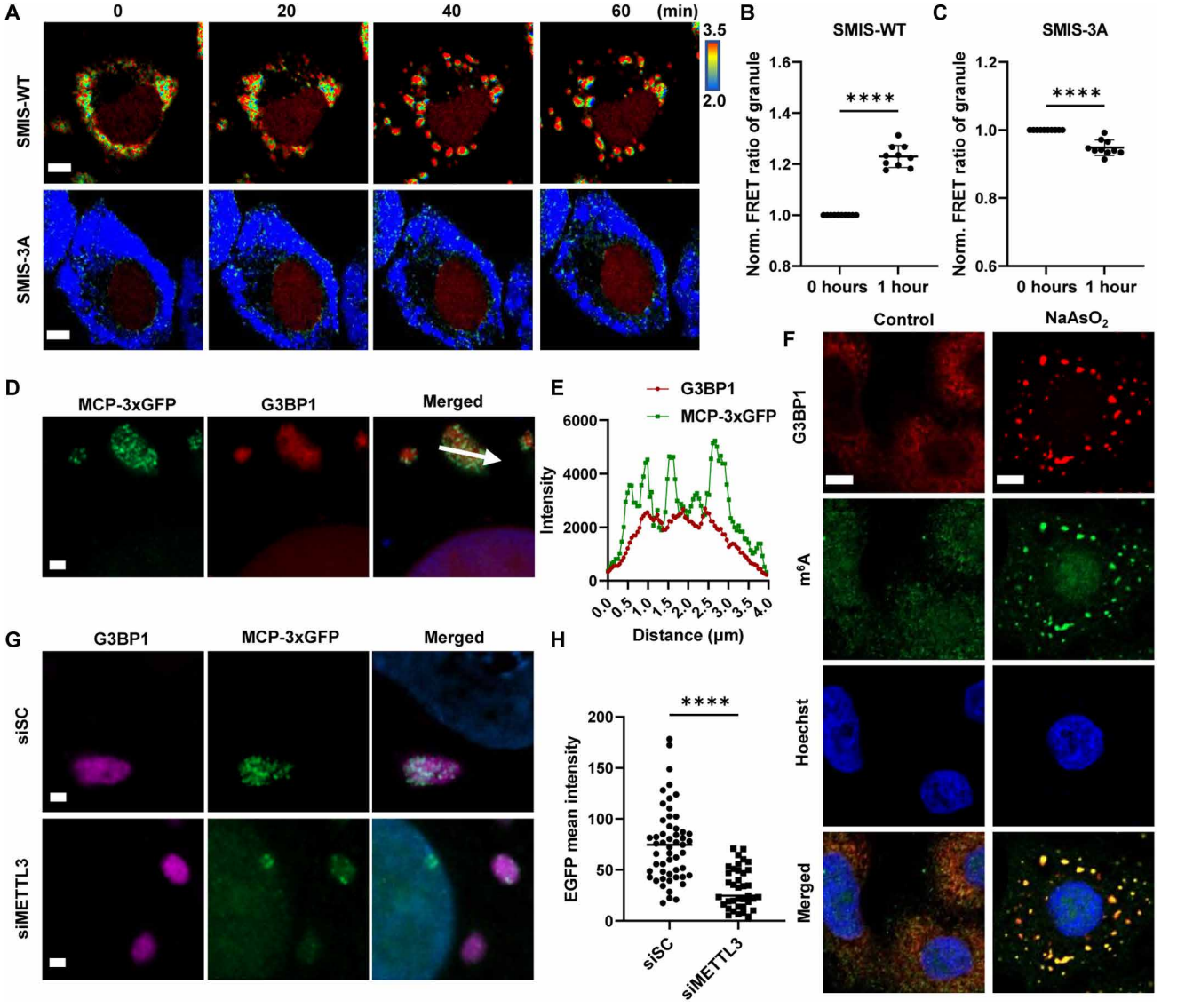

Fig. 5. m^{6}A modification promotes RNA accumulation in SGs. (**A**) Representative time-lapse images of the FRET ratio of SMIS-WT and SMIS-3A after DOX induction for 12 hours and $NaAsO_2$ treatment at the indicated time points. Scale bars, 5 μm. Normalized FRET ratio on granules in SMIS-WT (**B**) or SMIS-3A (**C**) after DOX induction for 12 hr and $NaAsO_2$ treatment for 1 hour. One dot represents the average FRET ratio of granules per cell after $NaAsO_2$ treatment normalized to the cytosolic FRET ratio in the same cell before $NaAsO_2$ treatment. Unpaired *t* test with Welch's correction (SMIS-WT: $n = 10$, $P < 0.0001$; SMIS-3A: $n = 10$, $P < 0.0001$). (**D**) MCP-3 × GFP and G3BP1 images in m^{6}A reporter cells after transient transfection of m^{6}A reporter cells with MCP-3×GFP for 36 hours, DOX induction for 12 hours, and $NaAsO_2$ treatment for 1 hour. The white arrow shows the quantification path. Scale bar, 1 μm. (**E**) G3BP1 and MCP-3×GFP intensity profiles are shown along the arrow in (D). (**F**) G3BP1 and m^{6}A immunostaining images in HeLa cells after $NaAsO_2$ treatment for 1 hour. Scale bars, 5 μm. (**G**) MCP-3×GFP and G3BP1 images in m^{6}A reporter cells after transient transfection with MCP-3×GFP for 12 hours, siSC or siMETTL3 treatment for 24 hours, DOX induction for 12 hours, and $NaAsO_2$ treatment for 1 hour. Scale bars, 2 μm. (**H**) EGFP mean intensity in SGs, as indicated by G3BP1-GFP puncta, after siSC or siMETTL3 treatment from (G). Unpaired *t* test with Welch's correction (siSC: $n = 53$; siMETTL3: $n = 37$; $P < 0.0001$).

group than in the control group (Fig. 5, G and H). Together, the live-cell imaging data from SMIS and immunostaining data strongly demonstrated that m^{6}A modification facilitated the partitioning of mRNAs into SGs under stress.

SMIS detects changes in SG stability and function regulated by siYTHDF2

Previous studies have shown that YTHDF1/2/3 could be associated with multiple m^{6}A-modified RNAs and undergo LLPS to form droplets in vitro (*27*). Knocking down YTHDF1/3 impaired SG formation, while knocking down YTHDF2 exhibited a limited effect (*28*). In general, information on the potential regulatory functions of YTHDFs in SG disassembly is limited. Here, we focused mainly on the function of YTHDFs in SG disassembly. First, we screened small interfering RNAs (siRNAs) against cytosolic readers of m^{6}A, including YTHDF1/2/3, and identified the siRNA that most strongly suppressed each specific reader gene (fig. S5, A to C). Then, we explored the regulatory effect of YTHDF1/2/3 on SG disassembly by

immunostaining for G3BP1 after siRNA treatment (fig. S5D). We found that only siYTHDF2 accelerated the SG disassembly process (Fig. 6, A and B). siYTHDF1 exhibited no effect on the disassembly process, and siYTHDF3 inhibited this process (fig. S5E). Using SMIS, we monitored the dynamics of m^6A modification, SG formation, and translation events simultaneously to address the role of YTHDF2 in SG stability and function. First, to demonstrate the feasibility of the SMIS system for studying SG dynamics in living cells, we carefully confirmed that the FRET biosensor and G3BP1 colocalized by performing immunostaining during SG formation and disassembly after siRNA treatment (fig. S6A). Then, we tracked the FRET changes and mMaroon1 intensities during dynamic SG processes. Along with the workflow (fig. S6B), SMIS exhibited dynamic granule formation after $NaAsO_2$ was added in the siSC group but exhibited markedly less granule formation in the siYTHDF2 group, suggesting that siYTHDF2 may inhibit granule formation (fig. S6C). Moreover, SMIS revealed that faster SG disassembly and FRET reduction occurred in SGs upon YTHDF2 knockdown (Fig. 6, C to E). All the live-cell imaging data demonstrated that knocking down YTHDF2 decreased SG stability and promoted the demethylation of

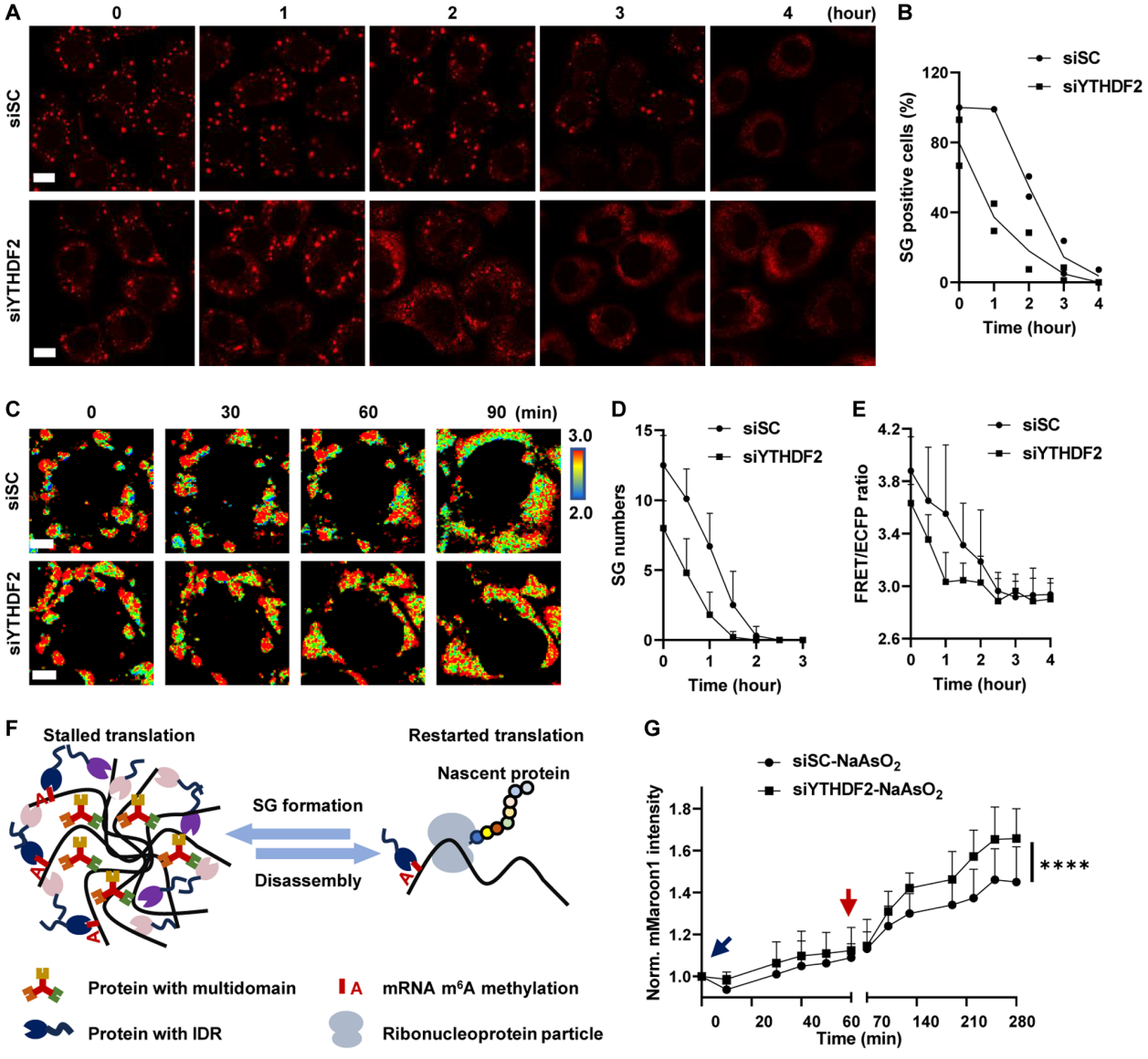

Fig. 6. YTHDF2 regulates SG stability and function. (**A**) G3BP1 immunostaining of HeLa cells after $NaAsO_2$ removal. HeLa cells were treated with siSC or siYTHDF2 for 48 hours, $NaAsO_2$ for 1 hour, and fresh medium supplemented with siRNA for the indicated times. Scale bars, 10 μm. (**B**) Percentage of SG-positive HeLa cells after $NaAsO_2$ removal. $n = 2$. (**C**) Representative images of the FRET ratio of SMIS-WT after siSC or siYTHDF2 treatment for 36 hours, DOX induction for 12 hours, $NaAsO_2$ treatment for 1 hour, and recovery by removal of $NaAsO_2$. Scale bars, 5 μm. (**D**) SG numbers in SG-positive SMIS-WT cells after $NaAsO_2$ removal from (C). $n = 8$. (**E**) Quantification of FRET ratio during SG disassembly in SMIS-WT cells after $NaAsO_2$ removal from (C). Granules were manually segmented and circled to quantify their average FRET/ECFP ratio at $t = 0$. As time went by, the average FRET/ECFP ratio in those circled regions were calculated continually regardless of whether granules were present or not. $n = 8$. (**F**) Relationships between translation and SG dynamics. (**G**) Normalized mMaroon1 intensity in SMIS-WT cells after siRNA treatment during SG formation and disassembly. Unpaired *t* test with Welch's correction ($n = 30$, $P < 0.0001$).

m^{6}A-modified RNAs, resulting in the redistribution of mRNAs into the cytosol. Furthermore, translational stalling is usually associated with SG formation (Fig. 6F) (*45*, *46*). In the SMIS, the translation of mMaroon1 in the siSC and siYTHDF2 groups was inhibited after $NaAsO_2$ treatment (fig. S6, D to F), and translation of the mMaroon1 mRNA trapped in SGs started as early as 0.5 hours after $NaAsO_2$ was removed. The siYTHDF2 group exhibited a relatively greater translation speed during SG recovery (Fig. 6G). The quick recovery of translation may benefit from rapid SG disassembly after YTHDF2 knockdown. In summary, SMIS revealed that YTHDF2 played important roles in promoting SG stability and function.

m^{6}A-modified RNA mediates the interaction between YTHDF2 and G3BP1 to maintain SG stability

To test the universality of YTHDF2-induced effects on the stability of SG, we knocked down YTHDF2 in U2OS cells that stably expressed EGFP-tagged G3BP1 (G3BP1-EGFP) and observed consistent results, as SG formation was reduced and SG disassembly was accelerated via siYTHDF2 treatment (Fig. 7, A and B, and fig. S7, A and B). G3BP1 is the critical protein in SG assembly (*47*), and double knockout (KO) of G3BP1/2 prevents $NaAsO_2$-induced SG formation (*23*). Thus, knocking down YTHDF2 might change SG stability through G3BP1.

We first quantified the protein level of G3BP1, and the results showed that siYTHDF2 efficiently reduced the YTHDF2 level and slightly increased the G3BP1 level (Fig. 7, C and D). Next, we investigated the interaction between YTHDF2 and G3BP1 because in addition to the YTH domain, YTHDF2 contains an intrinsically disordered region (IDR) that mediates various protein-protein interactions, as reported previously (*19*, *48*). Our co-immunoprecipitation (co-IP) results demonstrated that YTHDF2 interacted with G3BP1, and this interaction was strongly dependent on the presence of RNA (Fig. 7, E and F). Moreover, METTL3 knockdown significantly reduced the interaction between YTHDF2 and G3BP1, indicating that YTHDF2 interacted with G3BP1 in a m^{6}A-modified RNA-dependent manner (Fig. 7, G and H). The interaction of YTHDF2 and G3BP1 under unstressed condition was further confirmed by PLA (Fig. 7, I and J). Moreover, the colocalization between YTHDF2 and G3BP1 was further imaged via expansion microscopy with super-resolution (Fig. 7, K and L). YTHDF2 colocalized with G3BP1 under physiological conditions, with an ~0.8 Manders's colocalization coefficient. $NaAsO_2$ treatment caused YTHDF2 and G3BP1 to form larger granules and significantly increased the colocalization ratio. Knockdown of YTHDF2 increased the mobility of SGs (Fig. 7, M to O), demonstrating that the participation of YTHDF2 in SGs changed the biophysical properties of the granules, which might be related to interactions involving its IDR. In summary, we showed that the m^{6}A-modified RNA-mediated interaction between YTHDF2 and G3BP1 contributed to the stability and function of SG. Although knocking down YTHDF2 did not reduce the G3BP1 level, it might impair the multivalent interaction between m^{6}A-modified RNA and RNA binding proteins, thus reducing the stability of SGs and affecting the functions of SGs (Fig. 7P).

DISCUSSION

Here, we developed a SMIS system that dynamically visualized mRNA m^{6}A modifications in living cells. Our technology offered a powerful tool to generate high spatial and temporal resolution images of m^{6}A dynamics and functions in physiological and pathological processes, e.g., RNA transcription and translation. With SMIS, we found that the m^{6}A-modified reporter mRNAs tended to be enriched in SGs (Fig. 5), confirming that m^{6}A modification contributed to the partitioning of RNA during SG formation. After YTHDF2 knockdown, the SMIS showed that the stability of SGs decreased and that the translation recovery process accelerated during SG disassembly (Fig. 6). This is the first study to reveal the regulatory effect of YTHDF2 on SG disassembly. We further investigated the underlying mechanism, and the results revealed that the interaction between YTHDF2 and G3BP1 was dependent on m^{6}A-modified RNA (Fig. 7). Presumably, IDRs in YTHDF2 and m^{6}A-modified RNA mediate multivalent interactions between proteins and between protein and RNA to regulate SG stability and function (*19*, *23*, *29*, *47*). Owing to its high sensitivity and specificity in reporting m^{6}A at spatiotemporal resolution, SMIS can be applied to track, in principle, any m^{6}A-mediated RNA metabolic processes in living cells.

Recently, researchers demonstrated that another genetically encoded m^{6}A sensor system, called GEMS, can sense changes in m^{6}A methylation within living cells through using a YTH-APOBEC1 editable GFP reporter (*34*). When the mRNA of the GFP reporter was m^{6}A modified, YTH-APOBEC1 could recognize the m^{6}A modification and edit the adjacent C to U to form two stop codons, further preventing the expression of a destabilization domain after GFP. Although GEMS can be used to transform the m^{6}A level of reporter mRNA to GFP intensity as a simple readout, this method reads the m^{6}A level globally and at specific times without providing accurate spatiotemporal information. In contrast to GEMS, SMIS can perform time-lapse imaging and reveal the three-dimensional location of m^{6}A modifications (Figs. 4 to 6), which is critical for RNA function (*49*). In addition, YTH-APOBEC1 theoretically edits C on reporter mRNA and endogenous RNAs, which might change endogenous gene expression and function. SMIS monitors m^{6}A dynamics without affecting RNA sequence. Therefore, SMIS could provide more diversified applications; for instance, SIMS could track the reporter mRNA location and m^{6}A modification during SG formation and disassembly without editing endogenous RNAs.

The function of m^{6}A modification in guiding mRNAs into SGs is unclear. The earliest report on this topic showed that the mRNAs in SGs presented more m^{6}A modifications, as determined by quantifying the m^{6}A ratio through thin-layer chromatography and sequencing (*27*). In contrast, one study used single-molecule FISH analysis of 14 mRNAs and did not find different enrichment of those transcripts in WT and METTL3 KO cells, which suggested that m^{6}A modification had limited effects on the distribution of mRNAs into SGs (*31*). A recent study did the critical experiment of examining mRNA enrichment in SGs of METTL3 KO cells, showing definitively that m^{6}A guided enrichment of mRNAs into SGs (*50*). Nevertheless, it would be valuable to provide additional data using alternative approaches to further test the role of m^{6}A in mRNA enrichment in SGs. Our SMIS system directly monitors changes in the m^{6}A level in single living cells and largely remedies the heterogeneities of current methods, which are based on cell lysis and purification steps. SMIS reveals that the FRET ratio on SGs gradually increases during stress (Fig. 5A), which provides direct evidence that the average m^{6}A level on reporter mRNAs in SGs increases. Therefore, to some extent, our FRET imaging data support the

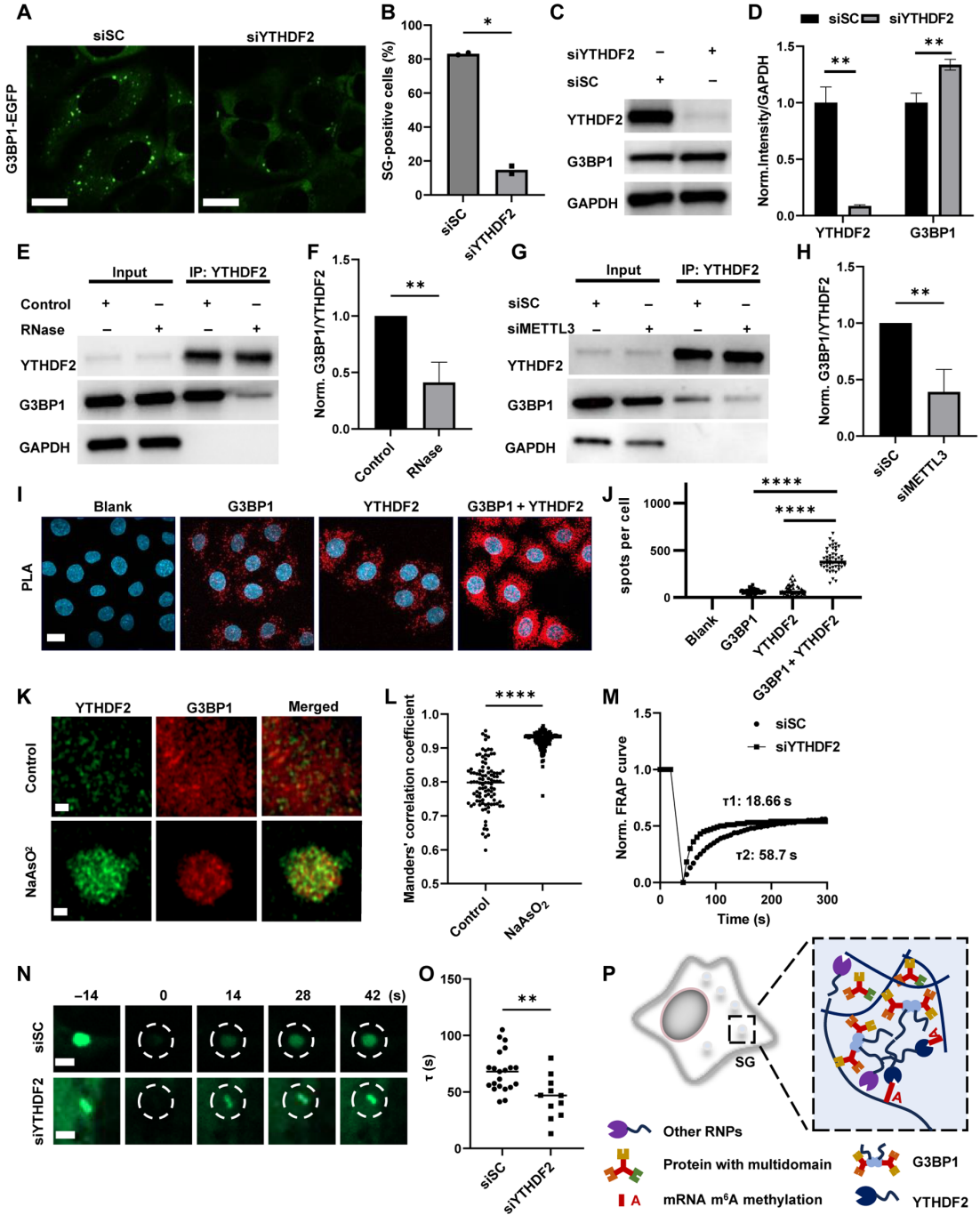

Fig. 7. YTHDF2 regulates the stability of SGs by interacting with G3BP1. EGFP images (**A**) and percentage of SG-positive cells (**B**) in U2OS G3BP1-EGFP after siRNA treatment for 48 hours and $NaAsO_2$ incubation for 1 hour. Scale bars, 15 μm. Cells with visible puncta labeled by EGFP in cytosol were counted as SG-positive cells. Unpaired *t* test with Welch's correction ($n = 2$, $P = 0.0136$). (**C**) Protein levels of G3BP1, YTHDF2, and GAPDH in HeLa cells with or without siRNA treatment were determined via Western blot (WB). (**D**) Normalized YTHDF2/GAPDH and G3BP1/GAPDH intensities in (C). $n = 3$, unpaired *t* test with Welch's correction (YTHDF2: $P = 0.0073$ and G3BP1: $P = 0.0079$). (**E**) Protein levels of G3BP1, YTHDF2, and GAPDH determined by WB after YTHDF2 pulling down in HeLa cells with or without RNase treatment. (**F**) Normalized G3BP1/YTHDF2 intensity in (E). Unpaired *t* test with Welch's correction ($n = 3$, $P = 0.0071$). (**G**) Protein levels of G3BP1, YTHDF2, and GAPDH determined by WB after YTHDF2 pulling down in HeLa cells treated with siSC or siMETTL3. (**H**) Normalized G3BP1/YTHDF2 intensity in (G). Unpaired *t* test with Welch's correction ($n = 4$, $P = 0.0087$). (**I**) PLA assays in HeLa cells incubated with/without G3BP1/YTHDF2 primary antibody. Scale bar, 10 μm. (**J**) Number of spots per cell in PLA assays. Unpaired *t* test with Welch's correction ($n = 50$, $P < 0.0001$). (**K**) Expansion microscopy of YTHDF2 and G3BP1 with/without $NaAsO_2$ treatment for 1 hour. Scale bars, 1 μm. (**L**) Manders' values for interaction between G3BP1 and YTHDF2 in (K). Unpaired *t* test with Welch's correction ($n = 101$, $P < 0.0001$). (**M**) Normalized FRAP curves of G3BP1-EGFP (dashed circles) in G3BP1-EGFP U2OS after siRNA treatment during FRAP. (**N**) G3BP1-EGFP images in (M). Scale bar, 1 μm. (**O**) τ of FRAP in (M). Unpaired *t* test with Welch's correction (siSC: $n = 21$; siYTHDF2: $n = 11$; $P = 0.0036$). (**P**) Schematic graph of multi-interaction between m^6A modification, YTHDF2, and SG-related proteins.

positive function of m^{6}A modification in the partitioning of mRNAs into SGs.

The function of m^{6}A readers in SG regulation has received much attention in recent years. In vitro studies have shown that YTHDF1/2/3 and their IDRs at the N terminus can undergo LLPS (*27*, *29*), and their C-terminal m^{6}A-binding domains also contribute to this process (*30*). The addition of multiple m^{6}A-modified RNAs notably exacerbates the LLPS process (*27*). However, the potential function and mechanism of YTHDF2 in regulating the stability of SGs in living cells remain unknown. Our results demonstrated that the knockdown of YTHDF2 markedly reduced the number of SGs, as indicated by G3BP1-GFP puncta, under $NaAsO_2$-induced stress (Fig. 7, A and B). Moreover, the reduction in YTHDF2 increased SG disassembly and m^{6}A-modified RNA partitioning into the cytosol, which further increased the translational recovery of SG-trapped mRNAs (Fig. 6, C to G). According to the results obtained with the SIMS system, YTHDF2 plays important roles in SG stability and function. Previous immunostaining revealed that YTHDF2 colocalized more with G3BP1 clusters, while YTHDF1/3 resided in the periphery of G3BP1 clusters in stressed cells (*28*). We believe that the siRNA chosen greatly affects the ability to efficiently reduce YTHDF2 levels, so we screened five siRNAs for YTHDF2 and selected the most efficient one with the minimum transcript level for functional study (fig. S5B). In addition, the expression level of YTHDF1/2/3 in distinct cells might determine which reader is responsible for m^{6}A-related functions in SG stability. For example, in a previous study, although the knockdown of YTHDF2 did not reduce SG formation, the overexpression of YTHDF2 rescued the siYTHDF1/3-induced reduction in SG yield (*28*).

In summary, the SMIS system provides substantial insight into the interplay between m^{6}A modification and SG stability by directly visualizing m^{6}A dynamics involved in the formation and disassembly of SGs in single living cells. SMIS shows advantages in tracking the location and dynamics of m^{6}A-modified reporter mRNA at high spatiotemporal resolution. In theory, SMIS can be applied to track any m^{6}A-mediated RNA metabolic processes in living cells. Several optimization steps can be performed when SMIS is applied to live-cell imaging. First, the current version of SMIS tracks transcription, m^{6}A modification, and translation of reporter mRNA but not endogenous mRNA. An antisense RNA or Cas13-targeting strategy could be used to perform m^{6}A imaging of endogenous mRNAs. Second, SMIS requires two components for m^{6}A detection by FRET. The copy number of the reporter mRNA and FRET biosensor may affect the sensitivity of the system because excess FRET biosensors may generate background signals if the sensors do not bind to RNAs. Therefore, delivering more reporter mRNAs or circularly permuted EGFP (cpEGFP)–based designs would be helpful.

MATERIALS AND METHODS

Plasmid construction for *Escherichia coli* expression

The pRSET B vector was linearized with Bam H1 and Eco R1 enzymes. The MCP fragment was amplified from pHAGE-EFS-MCP-3×BFP (Addgene, 75384). The ECFP fragment was amplified from the H3K9me3 FRET biosensor (BS) (*39*) (published in 2018 by our laboratory). MCP, ECFP, and linearized pRSET B were assembled with the ClonExpress Ultra One Step Cloning Kit (Vazyme, C115-01) to generate the pRSET B MCP-ECFP plasmid. YTH and YTH 3A fragments were amplified from pUC kan$^+$ YTH and YTH-3A (purchased from GENEWIZ Inc.), respectively. The YPet fragment was amplified from the H3K9me3 FRET BS. After YTH or YTH 3A, YPet and linearized pRSET B were assembled, and the pRSET B YTH-YPet and YTH-YPet 3A plasmids were generated.

Protein expression and purification

The pRSET B vectors containing MCP-ECFP, YTH-YPet, and YTH-YPet 3A were transformed into BL21 competent cells. A single colony was cultured overnight in 10 ml of LB medium supplemented with ampicillin. Two hundred milliliters of fresh LB medium was added to the culture medium, and the mixture was grown until the optical density was 2.0. Then, 0.2 mM isopropyl-β-D-thiogalactopyranoside was added to induce protein expression at 18°C for 20 hours. The bacteria were harvested and lysed in tris buffer [50 mM tris, 300 mM NaCl (pH 8.0), and 1× phenylmethylsulfonyl fluoride] by a homogenizer. The supernatant was collected after centrifugation at 20,000*g* for 30 min and incubated with pretreated Ni–nitrilotriacetic acid (Sangon Biotech, C600033) at 4°C for 1 hour. After the beads were carefully washed, the protein of interest was eluted with 300 mM imidazole. The elution buffer was changed to tris buffer [50 mM tris and 300 mM NaCl (pH 8.0)] through Amicon Ultra 15-ml Centrifugal Filters (Merck).

In vitro FRET assay

Before use, the RNA samples were heated at 85°C for 3 min and immediately placed on ice. MCP-ECFP (2 μM) and YTH-YPet (4 μM) or YTH-YPet 3A (4 μM) were incubated with m^{6}A aRNA (1 μM; GENEWIZ) or aRNA (1 μM; GENEWIZ) in RNA binding buffer [100 mM tris, 80 mM KCl, 10 mM $MgCl_2$, 1 mM dithiothreitol (DTT), 10% glycerol, and bovine serum albumin (BSA) (100 μg/ml)] at room temperature (RT) for 1 hour. The m^{6}A aRNA sequence used was CCGG/m^{6}A/CUGUACAUGAGGAUCACCCAUGU, and the aRNA sequence used was CCGGACUGUACAUGAGGAUCACCCAUGU. The fluorescent emission spectrum was tested by a Multimode Microplate Reader (Synergy H1, BioTek) after excitation at 420 nm. For the METTL3/14 catalysis assay, MCP-ECFP (2 μM), YTH-YPet (4 μM), and aRNA (1 μM) were mixed in reaction buffer [25 mM tris, 150 mM NaCl, 5% glycerol, 1 mM DTT, and RNase inhibitor (0.2 U/μl)] before METTL3/14 (0/0.5/1/2 μM) and SAM (10 μM) were added. After excitation at 420 nm, the kinetic emission at 528 nm and 478 nm was monitored.

Electrophoretic mobility shift assay

A mixture of RNA binding proteins and RNA was subjected to 10% native polyacrylamide gel electrophoresis in 1× tris-borate EDTA buffer. Electrophoresis was conducted at 120 eV for 60 min. The native gel was stained with Gel Red and imaged on a ChemiDoc MP imaging system (Bio-Rad). For MCP-ECFP association with RNA, MCP-ECFP (1 μM) was incubated with m^{6}A aRNA (1 μM) or aRNA (1 μM) in RNA binding buffer [100 mM Tris, 80 mM KCl, 10 mM $MgCl_2$, 1 mM DTT, 10% glycerol, and BSA (100 μg/ml)] for 1 hour before being directly loaded into the native gel. For YTH-YPet association with RNA, YTH-YPet (4 μM) was incubated with m^{6}A aRNA (1 μM) or aRNA (1 μM) in RNA binding buffer for 1 hour before being directly loaded into the native gel. For the METTL3/14 catalysis assay, after 12 hours, the reaction mixtures were directly loaded into native gels.

m^{6}A dot blot

The RNAs were extracted from the METTL3/14 catalysis solution by RNA Clean & Concentrator-5 (Zymo Research, R1013). The

RNA was further unfolded by heating at 85°C for 3 min and immediately incubated on ice. Forty-five nanograms of RNA was loaded on Hybond-N+ hybridization membranes (Merck, GERPN203B) and crosslinked by 365-nm ultraviolet (UV) light. The membrane was blocked with 5% BSA in Tris-Buffered Saline with 0.1% Tween-20 (TBST) and incubated with a m^6A antibody (1:200; Synaptic Systems, 202003) overnight. After three washes were performed with 1× TBST, the membrane was incubated with anti-rabbit immunoglobulin G (IgG) and horseradish peroxidase–linked antibodies [1:5000; Cell Signaling Technology (CST), 7074] at RT for 1 hour. Last, the membrane was washed thoroughly with 1× TBST and imaged with a ChemiDoc MP imaging system (Bio-Rad).

Cell culture and plasmid transfection

HeLa, U2OS, and G3BP1-GFP U2OS cells were cultured in Dulbecco's modified Eagle's medium (DMEM) supplemented with 10% Australian fetal bovine serum and 1% penicillin-streptomycin solution in a sterile 37°C incubator with 5% CO_2. For transient transfection, a Lipofectamine 3000 kit (Thermo Fisher Scientific, L3000015) was used according to the manufacturer's manual. Typically, we used 1.5 μl of Lipofectamine 3000 and 1 μl of P3000 to cotransfect 500 ng of reporter and 60 ng of BS plasmid into HeLa or U2OS cells.

Reporter plasmid construction

The mMaroon1 reporter plasmid was constructed by ligating dNLS-mMaroon1 cut by Nhe 1 and Kpn 1, the 22× m^6A-MS2 motif cut by Kpn 1 and Bam H1, and the linearized PLD1112 plasmid (a gift from Lin Deng) cut by Nhe 1 and Bam H1. dNLS-mMaroon1 was amplified from pLL3.7 m-mO2-SLBP-H1-mmaroon1 (previously constructed by our laboratory). The 22× m^6A-MS2 motif was cut from PUC kan^+ m^6A-MS2 (purchased from GENEWIZ Inc.). Similarly, a control reporter plasmid was constructed by replacing the m^6A-MS2 (GGAUC) motif with the control-MS2 motif GGTCU. The 22× control-MS2 motif was cut from PUC Kanamycin control-MS2 (purchased from GENEWIZ Inc.). The mCherry reporter plasmid was constructed via a similar strategy. All the ligation products were transformed into stbl3 competent cells, which were subsequently cultured at 30°C for further processing steps, including colony selection, plasmid extraction, and sequencing.

FRET biosensor construction

To rationally design SMIS system, we analyzed the structure of YTH domain and MCP protein. In the 3D structure of MCP protein, it forms dimer with head-to-tail orientation, and its N and C terminus are very close each other in the same direction, which determines the terminus position of MCP in the biosensor to avoid the high basal level of FRET. Meanwhile, N and C terminus of YTH domain are also on the same side, suggesting its terminal position in the biosensor as well. The affinity between YTH domain and m^6A-modified RNA is about 1.2 μM (*51*), which is good for biosensor design. Thus, we put the YTH domain at the N terminus and MCP at the C terminus with the canonical FRET pair YPet/ECFP in the middle. To obtain a sensitive FRET biosensor, we optimized linkers of FRET biosensor flanking by ECFP and YPet, MCP format, and copy number of NLS signal peptides. For the linker, we optimized with either the flexible EV linker (*35*) or semi-flexible linker 76 (*52*). For the MCP format, we tried the MCP monomer and the tandem dimeric MCP to evaluate the influence of MCP dimerization. We also designed cytosolic version of the FRET biosensor to allow measurement of m^6A modification in different subcellular locations.

The WT FRET biosensor (BS-WT) was constructed by assembling the YTH domain, YPet-EV-ECFP, MCP, and pSin vectors cut by Nhe 1 and Eco R1. The YTH domain (380 to 579 amino acids of YTHDF2) was amplified from pUC Kan^+ YTH (purchased from GENEWIZ Inc.). YPet-EV-ECFP was amplified from the H3K9me3 FRET BS (published in 2018 by our laboratory). MCP was amplified from pHAGE-EFS-MCP-3×BFP (Addgene, 75384). A mutant FRET biosensor (BS-3A) was constructed by replacing the YTH domain with the YTH-3A domain with the W432A, W486A, and W491A mutations. The YTH-3A domain was amplified from pUC Kan^+ YTH-3A (purchased from GENEWIZ Inc.). All the assembly products were transformed into DH5α competent cells, which were subsequently cultured at 37°C for further identification.

Virus packaging and infection

Human embryonic kidney (HEK) 293T cells were plated in 35-mm dishes at a cell density of approximately 40% on day 0. VSV-G (742 ng), delta-R8.2 (1536 ng), and the plasmid of interest (1.5 equivalent to VSV-G) were transfected into HEK293T cells by using the Lipofectamine 3000 kit on D1 according to the manufacturer's manual. At 6 hours after transfection, the medium was replaced with fresh medium. At 48 hours after transfection, the supernatant was collected and concentrated with PEG-it Virus Precipitation Solution (SBI, LV810A-1). The concentrated virus was stored in a −80°C freezer. For virus infection, HeLa cells were plated on 24-well plates and incubated with virus solution for 48 hours after adherence. The monoclonal cells with correct expression of the protein of interest were sorted by flow cytometry (FACS Aria III, BD Biosciences).

FRET imaging

FRET imaging was conducted on a Dragonfly Confocal Microscopy System equipped with a seven-laser, Electron Multiplying Charge-Coupled Device (EMCCD) camera, and live-cell workstation. The ECFP and FRET channels were excited by a 445-nm laser. The 478-nm filter and 571-nm filter were used to collect the emission of ECFP and FRET, respectively. The mMaroon1 was excited by a 637-nm laser, while a 698-nm filter was used to collect the emission. A multiposition model with a time series was used to track the live cells dynamically. The FRET ratio was calculated and displayed by the open-source software Fluocell (http://github.com/lu6007/fluocell) (*53*). For HeLa cells transiently transfected with the SMIS system, the cells were transported into glass-bottom dishes after 24 hours of transfection. The FRET images were acquired at least 12 hours after the cells were adherent. The settings of the ECFP and FRET channels were a 10% laser with a 100-gain value and 500-ms exposure time. The mMaroon1 channel was imaged with a 5% laser, 100 gain, and 500-ms exposure time. The cells with an ECFP intensity of 1000 to 1500 were counted to calculate the FRET ratio.

Immunostaining

The cells were plated on glass-bottom dishes and fixed with 4% paraformaldehyde for 30 min at least 12 hours after the cells had adhered. Then, the cells were permeabilized with 0.25% Triton in phosphate-buffered saline (PBS) for 30 min and blocked with 5% BSA in 1× Phosphate Buffered Saline with 0.1% Tween 20 (PBST) for 2 hours. The cells were incubated with antibodies against

METTL3 (1:1000; Abcam, ab195352), G3BP (1:1000; Abcam, ab56574), YTHDF2 (1:1000; Abcam, ab246514), or m^6A (1:200; Synaptic Systems, 202003) at 4°C overnight. Then, the cells were washed with 1× PBST three times and incubated with anti-mouse or anti-rabbit IgG antibodies conjugated with Alexa Fluor 594 for 1 hour. The nuclei were stained with Hoechst 33342 for 10 min.

siRNA treatment

Cells at 30 to 40% confluence were transfected with siRNA with Lipofectamine RNAiMAX (Thermo Fisher Scientific, 13778150) according to the manufacturer's recommendations. Typically, 3 μl of RNAiMAX reagent and 1 μl of siRNA stock (10 μM) were mixed with 50 μl of opti-MEM and incubated for 5 min at RT. The mixture was added to 1 ml of cell culture medium to induce protein knockdown with 0.5 million cells at most. For Western blotting and immunostaining, siRNA treatment was usually administered for 48 hours unless otherwise indicated. For SG formation in FRET imaging, siRNA treatment was usually performed for 36 hours, after which fresh medium containing DOX (1 μg/ml) and new siRNA was added to replace the original medium. For SG disassembly, fresh medium with new siRNA was added to replace the culture medium with $NaAsO_2$. The sequences of the siRNAs used are as follows: siSC (UUCUCCGAACGUGUCACGUTT), siMETTL3 (CGACUACAGUAGCUGCCUUTT), siYTHDF1 (GCGTCTAGTTGTTCATGAATT), siYTHDF2-1 (GGACGTTCCCAATAGCCAATT), siYTHDF2-2 (GCACAGAAGUUGCAAGCAATT), siYTHDF2-3 (GGGAUUGACUUCUCAGCAUTT), siYTHDF2-4 (GCAGUGGGUUCGGUCAUAATT), siYTHDF2-5 (GCACAGAGCAUGGUAACAATT), and siYTHDF3 (GCAAUACAGUAGAUUUGAAUACCTT).

Co-immunoprecipitation

For RNA-dependent co-IP, 2 million cells were harvested and lysed with 400 μl of Pierce IP Lysis Buffer (Thermo Fisher Scientific, 87787) containing protease inhibitor cocktail (1:100; Roche, 4693132001) and RNase inhibitor (1:100; Thermo Fisher Scienitific, N8080119) on ice for 20 min. The lysed mixture was centrifuged at 850*g* for 10 min. Twenty-five microliters of Dynabeads Protein G (Thermo Fisher Scientific, 88802) was used to pretreat and incubate the mixture with the supernatant to preclear the cell lysis. The protein concentration in the supernatant was quantified by a bicinchoninic acid (BCA) kit. Two hundred micrograms of supernatant was incubated with 1 μg of the YTHDF2 antibody (Abcam, ab246514) for 1 hour at RT. Then, 50 μl of Dynabeads Protein G was added to the mixture, which was subsequently incubated for another hour. The beads were washed with Pierce IP Lysis Buffer three times and then separated equally into two tubes. One hundred microliters of lysis buffer containing RNase (10 μg/ml) or RNase inhibitor (1:100) was incubated with the beads for 30 min. The beads were washed with Pierce IP Lysis Buffer three times. Then, 20 μl of 1× loading buffer was incubated with the beads and heated at 95°C for 10 min. To identify the proteins, Western blot analysis was performed with YTHDF2 (1:1000; Abcam, ab246514), G3BP (1:1000; Abcam, ab56574), and glyceraldehyde-3-phosphate dehydrogenase (GAPDH) (1:5000; CST, 2118). For m^6A-dependent Co-IP, HeLa cells treated with siSC or siMETTL3 for 48 hours were lysed with 200 μl of Pierce IP lysis buffer containing protease inhibitor cocktail and RNase inhibitor (1:100) on ice for 20 min. The subsequent procedures followed the above co-IP protocol.

Fluorescence recovery after photobleaching

G3BP1-EGFP U2OS cells were treated with siRNA for 48 hours and $NaAsO_2$ for 1.5 hours and imaged by SpinSR (Olympus). The fluorescence recovery after photobleaching (FRAP) workflow included 5 cycles of confocal imaging with a 488-nm laser, 5 cycles of photobleaching with 60% laser power of a 405-nm laser, and 50 cycles of continuous imaging with a 488-nm laser. The data were analyzed by the FRAP model of cellsens software with double exponential function fitting. The τ value indicates the recovery time after FRAP.

Expansion microscopy

The expansion microscope methods were performed according to the literature, with minor modifications (*54*). Specifically, HeLa cells were incubated with fixation solution for 15 min at RT and then washed with 1× PBS three times for 10 min each. The cells were treated with postfix solution in a gelation chamber for 6 to 7 hours at 37°C. Then, the cells were washed with PBS twice and incubated with expansion gel solution for 15 min at RT. The cells were subsequently incubated with expansion gel solution for 1.5 hours at 37°C. Coverslips with hydrogels were then incubated in 1 ml of denaturation buffer for 15 min at RT. The gels were then transferred into tubes filled with 1.5 ml of denaturation buffer and incubated at 73°C for 1 hour. Then, the gels were incubated with Milli-Q water in petri dishes overnight for expansion. In the first 2 hours of incubation, we changed the water every hour and then incubated with fresh water for overnight.

The fixation solution was 3% formaldehyde (FA) and 0.1% glutaraldehyde (GA) in 1× PBS. Postfix solution was 0.7% FA + 1% acrylamide (w/v) in 1× PBS. Expansion gel solution was 19% (w/v) sodium acrylate + 10% acrylamide (w/v) + 0.1% (w/v) *N*, *N*′-(1,2-dihydroxyethylene) bisacrylamide + 0.25% (v/v) Tetramethylethylenediamine (TEMED) + 0.25% (w/v) ammonium persulfate in 1× PBS. Denaturation buffer was 200 mM SDS + 200 mM NaCl + 50 mM tris in Milli-Q water (pH 6.8).

m6ACE library preparation

m6ACE library preparation was conducted according to literature (*41*) with minor modification. Specifically, the total RNA was extracted from cells using total RNA kit I (Omega Bio-tek, R6834) according to the manufacturer's instructions. Then, polyadenylate [poly(A)] RNA was purified by VAHTS mRNA Capture Beads 2.0 (Vazyme, N403-01). After ethanol precipitation, poly(A) RNA was fragmented by treatment with RNA fragmentation buffer (Ambion, AM8740) for 7.5 min at 70°C to form fragments of 120 to 150 nt in length. After another round of ethanol precipitation, fragmented RNA was incubated with 10 U of T4 PNK (NEB, M0201) for 30 min at 37°C. Then, 1 mM adenosine 5′-triphosphate (ATP) was added into the solution and incubated for 30 min at 37°C. Phosphorylated RNA was purified by Oligo Clean & Concentrator (Zymo Research, D4060) and ligated with 5′-adenylated,3-dideoxyC DNA adaptors by 400 U of truncated T4 RNA ligase 2 (NEB, M0242) in 1× ATP-free T4 RNA ligase buffer [50 mM tris (pH 7.5); BSA (60 μg/ml); 10 mM $MgCl_2$; 10 mM DTT; and 12.5% polyethylene glycol, molecular weight 800 (PEG-8000)] for 2 hours at 25°C. The 3′ ligation product was purified with AMPure XP beads (Beckman Coulter, A63881). A total of 200 pg of 3′-ligated methylated RNA spike-in was added to 1 to 5 μg of ligated poly(A) RNA, and the mixture was denatured for 5 min at 65°C before incubating for 2 min on ice. The denatured RNA was incubated overnight at 4°C with 8 μg of anti-m^6A

antibody (Synaptic Systems, 202003) in 1× IP buffer [150 mM LiCl, 10 mM tris (pH 7.4), and 0.1% IGEPAL CA-630 (Sigma-Aldrich I8896)] supplemented with RNasin Plus (1 U/μl; Promega N2611). In parallel, 1.2 mg of Dynabeads Protein A was blocked with BSA (0.5 mg/ml; Sigma-Aldrich, A7906) in 1× IP buffer overnight at 4°C. The antibody-RNA mixture was separated into 50 μl of aliquots and cross-linked six times with 254-nm UV radiation at 0.15 J/cm^2. The antibody-RNA mixture was recombined for further operation. The 1% of the mixture was used as input-RNA. The remainder (designated as m6ACE-RNA) was mixed with preblocked Dynabeads Protein A or 1.5 hours at 4°C. Beads were then washed with 250 μl of cold buffers as follows: wash buffer 1 [1 M NaCl, 50 mM Hepes-KOH (pH 7.4), 1% Triton X-100, 0.1% sodium deoxycholate, and 2 mM EDTA], wash buffer 2 [0.5 M NaCl, 50 mM Hepes-KOH (pH 7.4), 1% IGEPAL, 0.1% sodium deoxycholate, and 2 mM EDTA], wash buffer 3 [1% sodium deoxycholate, 25 mM LiCl, 10 mM tris (pH 8), 1% Triton X-100, and 2 mM EDTA], TE [10 mM tris (pH 8) and 1 mM EDTA], and lastly 10 mM Tris (pH 8). m6ACE RNA was then denatured in 10 μl of 10 mM tris (pH 8) for 5 min at 65°C and kept on ice. A total of 1 U of XRN-1 (NEB, M0338) was used as 5′ to 3′ exonuclease to digest m6ACE RNA in XRN-1 buffer [100 mM LiCl, 45 mM tris (pH 8), 10 mM $MgCl_2$, and 1 mM DTT] and RNasin Plus (1 U/μl), with shaking at 1000 rpm for 1 hour at 37°C. The m6ACE RNA-bead mixture was then washed with wash buffer 1, wash buffer 2, wash buffer 3, TE, and 10 mM tris (pH 8). Both input and m6ACE RNAs were eluted in elution buffer [1% SDS, 200 mM NaCl, 25 mM tris (pH 8), 2 mM EDTA, and Proteinase K (1 mg/ml; Thermo Fisher Scientific, EO0491)], with shaking at 1000 rpm for 1.5 hours at 50°C. RNAs were ethanol-precipitated and ligated to 5 pmol of 5′ adaptors with 10 U of T4 RNA ligase (Ambion, AM2140) supplemented with 12.5% PEG-8000 and RNasin Plus (2 U/μl) for 16 hours at 16°C before being purified with Oligo Clean & Concentrator. A total of 5 pmol of reverse transcription primer was annealed (72°C for 2 min, ice for 2 min), and reverse transcription was performed with 200 U of Superscript III (Invitrogen, 18080) for 1 hour at 50°C, with the reaction stopped by incubating for 15 min at 70°C. The cDNA was PCR-amplified for 14 cycles with Phusion High-fidelity PCR master mix (Thermo Fisher Scientific, F530) and TruSeq PCR primers. Last, primer-dimer and adaptor dimers were removed with AMPure XP beads before undergoing PE150 sequencing on the Illumina NovaSeq platform.

m6ACE-seq data analysis

m6ACE-seq analysis was performed as previously described: Fastq sequences were first filtered for a quality score of 20 and then trimmed of 5′ and 3′ adapter sequences and poly(A) tails using Cutadapt 3.7 -q 20 -m 30 -a TGGAATTCTCGGGTGCCAAGG -A GATCGTCGGACTGTAGAACTCTGAAC. The 8-nucleotide oligomer Unique Molecular Identifier (UMI) located at the first eight nucleotides of read 1 was registered and trimmed. Any complementary UMI sequence in read 2 was also trimmed. Reads were mapped to the methylated spike-in (rUrCrUrCrCrUrUrArGrUrArGrCrUrCrCrUrArArGm6ArUrCrGrUrCrGrArGrUrUrArCrArCrGrArCrGr-ArCrArUrUrGrUrUrCrCrGrArCrUrGrArCrG) or to the mMaroon1 reporter gene sequence using Bowtie2 2.2.5 -q -N 1 –no-mixed –no-discordant. Aligned pairs that had the same mapping coordinates and UMIs were filtered out as PCR duplicates. To calculate the relative methylation level (m6ACE/input) of each site, the read-start counts at the middle of each of the 22 "GGACU" m6ACE library were divided by the read-start counts at the same site in the input library.

Statistical analysis

Statistical analysis was performed using GraphPad Prism by unpaired *t* test with Welch's correction. ns (not significant), $P > 0.05$; *$P < 0.05$; **$P < 0.01$; ***$P < 0.001$; and ****$P < 0.0001$.

Supplementary Materials

This PDF file includes:

Figs. S1 to S7

REFERENCES AND NOTES

1. J. H. Lee, R. Y. Wang, F. Xiong, J. Krakowiak, Z. Liao, P. T. Nguyen, E. V. Moroz-Omori, J. F. Shao, X. Y. Zhu, M. J. Bolt, H. Y. Wu, P. K. Singh, M. J. Bi, C. J. Shi, N. Jamal, G. J. Li, R. Mistry, S. Y. Jung, K. L. Tsai, J. C. Ferreon, F. Stossi, A. Caflisch, Z. J. Liu, M. A. Mancini, W. B. Li, Enhancer RNA m6A methylation facilitates transcriptional condensate formation and gene activation. *Mol. Cell* **81**, 3368–3385.e9 (2021).
2. S. Deng, J. L. Zhang, J. C. Su, Z. X. Zuo, L. X. Zeng, K. J. Liu, Y. F. Zheng, X. D. Huang, R. H. Bai, L. S. Zhuang, Y. Ye, M. Li, L. Pan, J. G. Deng, G. D. Wu, R. Li, S. P. Zhang, C. Wu, D. X. Lin, J. J. Chen, J. Zheng, RNA m6A regulates transcription via DNA demethylation and chromatin accessibility. *Nat. Genet.* **54**, 1427–1437 (2022).
3. I. A. Roundtree, C. He, Nuclear m^{6}A reader YTHDC1 regulates mRNA splicing. *Mol. Cell* **61**, 507–519 (2016).
4. I. A. Roundtree, G. Z. Luo, Z. J. Zhang, X. Wang, T. Zhou, Y. Q. Cui, J. H. Sha, X. X. Huang, L. Guerrero, P. Xie, E. He, B. Shen, C. He, YTHDC1 mediates nuclear export of N^6-methyladenosine methylated mRNAs. *eLife* **6**, 31311 (2017).
5. X. Wang, Z. K. Lu, A. Gomez, G. C. Hon, Y. N. Yue, D. L. Han, Y. Fu, M. Parisien, Q. Dai, G. F. Jia, B. Ren, T. Pan, C. He, N^6-methyladenosine-dependent regulation of messenger RNA stability. *Nature* **505**, 117–120 (2014).
6. X. Wang, B. S. Zhao, I. A. Roundtree, Z. K. Lu, D. L. Han, H. H. Ma, X. C. Weng, K. Chen, H. L. Shi, C. He, N^6-methyladenosine modulates messenger RNA translation efficiency. *Cell* **161**, 1388–1399 (2015).
7. H. L. Huang, H. Y. Weng, W. J. Sun, X. Qin, H. L. Shi, H. Z. Wu, B. S. Zhao, A. Mesquita, C. Liu, C. L. Yuan, Y. C. Hu, S. Hüttelmaier, J. R. Skibbe, R. Su, X. L. Deng, L. Dong, M. Sun, C. Y. Li, S. Nachtergaele, Y. G. Wang, C. Hu, K. Ferchen, K. D. Greis, X. Jiang, M. J. Wei, L. H. Qu, J. L. Guan, C. He, J. H. Yang, J. J. Chen, Recognition of RNA N^6-methyladenosine by IGF2BP proteins enhances mRNA stability and translation. *Nat. Cell Biol.* **20**, 1098–1098 (2018).
8. Y. N. Li, X. Y. Dou, J. Liu, Y. Xiao, Z. Zhang, L. Hayes, R. Wu, X. J. Fu, Y. Z. Ye, B. Yang, L. W. Ostrow, C. He, S. Y. Sun, Globally reduced N^6-methyladenosine (m^{6}A) in C9ORF72-ALS/FTD dysregulates RNA metabolism and contributes to neurodegeneration. *Nat. Neurosci.* **26**, 1328–1338 (2023).
9. E. Yankova, W. Blackaby, M. Albertella, J. Rak, E. De Braekeleer, G. Tsagkogeorga, E. S. Pilka, D. Aspris, D. Leggate, A. G. Hendrick, N. A. Webster, B. Andrews, R. Fosbeary, P. Guest, N. Irigoyen, M. Eleftheriou, M. Gozdecka, J. M. L. Dias, A. J. Bannister, B. Vick, I. Jeremias, G. S. Vassiliou, O. Rausch, K. Tzelepis, T. Kouzarides, Small-molecule inhibition of METTL3 as a strategy against myeloid leukaemia. *Nature* **593**, 597–601 (2021).
10. M. McMillan, N. Gomez, C. R. L. E. Hsieh, M. Bekier, X. L. Li, R. Miguez, E. M. H. Tank, S. J. Barmada, RNA methylation influences TDP43 binding and disease pathogenesis in models of amyotrophic lateral sclerosis and frontotemporal dementia. *Mol. Cell* **83**, 219–236.e7 (2023).
11. X. L. Jiang, B. Y. Liu, Z. Nie, L. C. Duan, Q. X. Xiong, Z. X. Jin, C. P. Yang, Y. B. Chen, The role of m6A modification in the biological functions and diseases. *Signal Transduct. Target. Ther.* **6**, 74 (2021).
12. Y. Yang, P. J. Hsu, Y. S. Chen, Y. G. Yang, Dynamic transcriptomic m^{6}A decoration: Writers, erasers, readers and functions in RNA metabolism. *Cell Res.* **28**, 616–624 (2018).
13. K. D. Meyer, DART-seq: An antibody-free method for global m^{6}A detection. *Nat. Methods* **16**, 1275–1280 (2019).
14. Y. Wang, Y. Xiao, S. Q. Dong, Q. Yu, G. F. Jia, Antibody-free enzyme-assisted chemical approach for detection of N^6-methyladenosine. *Nat. Chem. Biol.* **16**, 896–903 (2020).
15. L. L. Hu, S. Liu, Y. Peng, R. Q. Ge, R. Su, C. Senevirathne, B. T. Harada, Q. Dai, J. B. Wei, L. S. Zhang, Z. Y. Hao, L. Z. Luo, H. Y. Wang, Y. R. Wang, M. K. Luo, M. J. Chen, J. J. Chen, C. He, m^{6}A RNA modifications are measured at single-base resolution across the mammalian transcriptome. *Nat. Biotechnol.* **40**, 1210–1219 (2022).
16. K. D. Meyer, Y. Saletore, P. Zumbo, O. Elemento, C. E. Mason, S. R. Jaffrey, Comprehensive analysis of mRNA methylation reveals enrichment in 3′ UTRs and near stop codons. *Cell* **149**, 1635–1646 (2012).

17. D. Dominissini, S. Moshitch-Moshkovitz, S. Schwartz, M. Salmon-Divon, L. Ungar, S. Osenberg, K. Cesarkas, J. Jacob-Hirsch, N. Amariglio, M. Kupiec, R. Sorek, G. Rechavi, Topology of the human and mouse m^{6}A RNA methylomes revealed by m^{6}A seq. *Nature* **485**, 201–206 (2012).
18. M. A. Garcia-Campos, S. Edelheit, U. Toth, M. Safra, R. Shachar, S. Viukov, R. Winkler, R. Nir, L. Lasman, A. Brandis, J. H. Hanna, W. Rossmanith, S. Schwartz, Deciphering the "m^{6}A code" via antibody-independent quantitative profiling. *Cell* **178**, 731–747.e16 (2019).
19. S. Zaccara, S. R. Jaffrey, A unified model for the function of YTHDF proteins in regulating m^{6}A modified mRNA. *Cell* **181**, 1582–1595.e18 (2020).
20. Z. Y. Zou, C. Sepich-Poore, X. M. Zhou, J. B. Wei, C. He, The mechanism underlying redundant functions of the YTHDF proteins. *Genome Biol.* **24**, 17 (2023).
21. Y. Gwon, B. A. Maxwell, R. M. Kolaitis, P. P. Zhang, H. J. Kim, J. P. Taylor, Ubiquitination of G3BP1 mediates stress granule disassembly in a context-specific manner. *Science* **372**, eabf6548 (2021).
22. K. Zhang, J. G. Daigle, K. M. Cunningham, A. N. Coyne, K. Ruan, J. C. Grima, K. E. Bowen, H. Wadhwa, P. G. Yang, F. Rigo, J. P. Taylor, A. D. Gitler, J. D. Rothstein, T. E. Lloyd, Stress granule assembly disrupts nucleocytoplasmic transport. *Cell* **173**, 958–971.e17 (2018).
23. P. G. Yang, C. Mathieu, R. M. Kolaitis, P. P. Zhang, J. Messing, U. Yurtsever, Z. M. Yang, J. J. Wu, Y. X. Li, Q. F. Pan, J. Y. Yu, E. W. Martin, T. Mittag, H. J. Kim, J. P. Taylor, G3BP1 is a tunable switch that triggers phase separation to assemble stress granules. *Cell* **181**, 325–345.e28 (2020).
24. C. McCormick, D. A. Khaperskyy, Translation inhibition and stress granules in the antiviral immune response. *Nat. Rev. Immunol.* **17**, 647–660 (2017).
25. C. McCormick, D. A. Khaperskyy, Single-molecule imaging reveals translation of mRNAs localized to stress granules. *Cell* **183**, 1801–1812.e13 (2020).
26. M. Anders, I. Chelysheva, I. Goebel, T. Trenkner, J. Zhou, Y. H. Mao, S. Verzini, S. B. Qian, Z. Ignatova, Dynamic m^{6}A methylation facilitates mRNA triaging to stress granules. *Life Sci. Alliance* **1**, e201800113 (2018).
27. R. J. Ries, S. Zaccara, P. Klein, A. Olarerin-George, S. Namkoong, B. F. Pickering, D. P. Patil, H. Kwak, J. H. Lee, S. R. Jaffrey, m^{6}A enhances the phase separation potential of mRNA. *Nature* **571**, 424–428 (2019).
28. Y. Fu, X. W. Zhuang, m^{6}A binding YTHDF proteins promote stress granule formation. *Nat. Chem. Biol.* **16**, 955–963 (2020).
29. Y. F. Gao, G. F. Pei, D. X. Li, R. Li, Y. Q. Shao, Q. C. Zhang, P. L. Li, Multivalent m^{6}A motifs promote phase separation of YTHDF proteins. *Cell Res.* **29**, 767–769 (2019).
30. J. H. Wang, L. Y. Wang, J. B. Diao, Y. G. Shi, Y. Shi, H. H. Ma, H. J. Shen, Binding to m^{6}A RNA promotes YTHDF2-mediated phase separation. *Protein Cell* **11**, 304–307 (2020).
31. A. Khong, T. Matheny, T. N. Huynh, V. Babl, R. Parker, Limited effects of m^{6}A modification on mRNA partitioning into stress granules. *Nat. Commun.* **13**, 3735 (2022).
32. X. J. Ren, R. J. Deng, K. X. Zhang, Y. P. Sun, Y. Li, J. H. Li, Single-cell imaging of m^{6}A modified RNA using m^{6}A specific in situ hybridization mediated proximity ligation assay (m^{6}AISH-PLA). *Angew. Chem. Int. Ed. Engl.* **60**, 22646–22651 (2021).
33. C. J. Sheehan, B. F. Marayati, J. Bhatia, K. D. Meyer, visualization of m^{6}A sites in cellular mRNAs. *Nucleic Acids Res.* **51**, e101 (2023).
34. B. F. Marayati, M. G. Thompson, C. L. Holley, S. M. Horner, K. D. Meyer, Programmable protein expression using a genetically encoded m^{6}A sensor. *Nat. Biotechnol.* **42**, 1417–1428 (2024).
35. N. Komatsu, K. Aoki, M. Yamada, H. Yukinaga, Y. Fujita, Y. Kamioka, M. Matsuda, Development of an optimized backbone of FRET biosensors for kinases and GTPases. *Mol. Biol. Cell* **22**, 4647–4656 (2011).
36. L. Hellweg, A. Edenhofer, L. Barck, M. C. Huppertz, M. S. Frei, M. Tarnawski, A. Bergner, B. Koch, K. Johnsson, J. Hiblot, A general method for the development of multicolor biosensors with large dynamic ranges. *Nat. Chem. Biol.* **19**, 1147–1157 (2023).
37. J. F. Zhang, B. Liu, I. Hong, A. L. Mo, R. H. Roth, B. Tenner, W. Lin, J. Z. Zhang, R. S. Molina, M. Drobizhev, T. E. Hughes, L. Tian, R. L. Huganir, S. Mehta, J. Zhang, An ultrasensitive biosensor for high-resolution kinase activity imaging in awake mice. *Nat. Chem. Biol.* **17**, 39–46 (2021).
38. L. W. Liu, P. Limsakul, X. H. Meng, Y. Huang, R. E. S. Harrison, T. S. Huang, Y. W. Shi, Y. Y. Yu, K. Charupanit, S. Zhong, S. Y. Lu, J. Zhang, S. Chien, J. Sun, Y. X. Wang, Integration of FRET and sequencing to engineer kinase biosensors from mammalian cell libraries. *Nat. Commun.* **12**, 5031 (2021).
39. Y. X. Wang, Q. Peng, Coordinated histone modifications and chromatin reorganization in a single cell revealed by FRET biosensors. *Proc. Natl. Acad. Sci. U.S.A.* **115**, E11681–E11690 (2018).
40. J. Z. Liu, Y. N. Yue, D. L. Han, X. Wang, Y. Fu, L. Zhang, G. F. Jia, M. Yu, Z. K. Lu, X. Deng, Q. Dai, W. Z. Chen, C. He, A METTL3-METTL14 complex mediates mammalian nuclear RNA N^6 adenosine methylation. *Nat. Chem. Biol.* **10**, 93–95 (2014).
41. C. W. Q. Koh, Y. T. Goh, W. S. S. Goh, Atlas of quantitative single-base-resolution -methyl-adenine methylomes. *Nat. Commun.* **10**, 5636 (2019).
42. L. J. Sun, Z. Y. Zuo, X. K. Qiu, G. X. Wang, Q. Q. Li, J. H. Qiu, Q. Peng, Recent advances in the interplay between stress granules and m^{6}A RNA modification. *Curr. Opin. Solid State Mater. Sci.* **27**, 101119 (2023).
43. Z. Q. Ren, W. Tang, L. X. Peng, P. Zou, Profiling stress-triggered RNA condensation with photocatalytic proximity labeling. *Nat. Commun.* **14**, 7390 (2023).
44. L. L. Jiang, W. W. Lin, C. Zhang, P. E. A. Ash, M. Verma, J. Kwan, E. van Vliet, Z. Yang, A. L. Cruz, S. Boudeau, B. F. Maziuk, S. W. Lei, J. Song, V. E. Alvarez, S. Hovde, J. F. Abisambra, M. H. Kuo, N. Kanaan, M. E. Murray, J. F. Crary, J. Zhao, J. X. Cheng, L. Petrucelli, H. Li, A. Emili, B. Wolozin, Interaction of tau with HNRNPA2B1 and N^6-methyladenosine RNA mediates the progression of tauopathy. *Mol. Cell* **81**, 4209–4227.e12 (2021).
45. S. R. Kimball, R. L. Horetsky, D. Ron, L. S. Jefferson, H. P. Harding, Mammalian stress granules represent sites of accumulation of stalled translation initiation complexes. *Am. J. Physiol. Cell Physiol.* **284**, 273–284 (2003).
46. A. Khong, T. Matheny, S. Jain, S. F. Mitchell, J. R. Wheeler, R. Parker, The stress granule transcriptome reveals principles of mRNA accumulation in stress granules. *Mol. Cell* **68**, 808–820.e5 (2017).
47. J. Guillén-Boixet, A. Kopach, A. S. Holehouse, S. Wittmann, M. Jahnel, R. Schlüssler, K. Kim, I. R. E. A. Trussina, J. Wang, D. Mateju, I. Poser, S. Maharana, M. Ruer-Gruss, D. Richter, X. J. Zhang, Y. T. Chang, J. Guck, A. Honigmann, J. Mahamid, A. A. Hyman, R. V. Pappu, S. Alberti, T. M. Franzmann, RNA-induced conformational switching and clustering of G3BP drive stress granule assembly by condensation. *Cell* **181**, 346–361.e17 (2020).
48. H. J. Hwang, T. L. Park, H. I. Kim, Y. Park, G. Kim, C. Y. Song, W. K. Cho, Y. K. Kim, YTHDF2 facilitates aggresome formation via UPF1 in an m^{6}A independent manner. *Nat. Commun.* **14**, 6248 (2023).
49. P. Anderson, N. Kedersha, RNA granules: Post-transcriptional and epigenetic modulators of gene expression. *Nat. Rev. Mol. Cell. Biol.* **10**, 430–436 (2009).
50. R. J. Ries, B. F. Pickering, H. X. Poh, S. Namkoong, S. R. Jaffrey, m^{6}A governs length-dependent enrichment of mRNAs in stress granules. *Nat. Struct. Mol. Biol.* **30**, 1525–1535 (2023).
51. T. T. Zhu, I. A. Roundtree, P. Wang, X. Wang, L. Wang, C. Sun, Y. Tian, J. Li, C. He, Y. H. Xu, Crystal structure of the YTH domain of YTHDF2 reveals mechanism for recognition of N^6-methyladenosine. *Cell Res.* **24**, 1493–1496 (2014).
52. Y. Ni, B. J. H. M. Rosier, E. A. van Aalen, E. T. L. Hanckmann, L. Biewenga, A. M. M. Pistikou, B. Timmermans, C. Vu, S. Roos, R. Arts, W. T. Li, T. F. A. de Greef, M. M. G. J. van Borren, F. J. M. van Kuppeveld, B. J. Bosch, M. Merkx, A plug-and-play platform of ratiometric bioluminescent sensors for homogeneous immunoassays. *Nat. Commun.* **12**, 4586 (2021).
53. Q. Qin, S. Laub, Y. W. Shi, M. X. Ouyang, Q. Peng, J. Zhang, Y. X. Wang, S. Y. Lu, *Fluocell* for ratiometric and high-throughput live-cell image visualization and quantitation. *Front. Phys.* **7**, 154 (2019).
54. O. M'Saad, J. Bewersdorf, Light microscopy of proteins in their ultrastructural context. *Nat. Commun.* **11**, 3850 (2020).

Acknowledgments: We thank Z. Li from Shenzhen Bay Laboratory for providing the METTL3/14 complex, H. Wang at Sun Yat-Sen University for providing STM2457, and P. Yang at Westlake University for providing the U2OS G3BP1-GFP cell line. We thank the Bio-imaging Core facility at Shenzhen Bay Laboratory for providing imaging support. We also would like to acknowledge engineers M. Yu and S. Huang from the Bio-imaging Core facility for assistance with laser-point scanning confocal microscopy (Zeiss 980) and Dragonfly Spinning Disk Confocal Microscopy (7 laser). **Funding:** This work was supported by the Guangdong Basic and Applied Basic Research Foundation (2024A1515012962 to Q.L.), the National Science Foundation of China (32100450 and 32471370 to Q.P.), the Guang-dong Pearl River Talent Program (2021QN02Y781 to Q.P.), and the SZBL-Evident/Olympus Imaging Technology Fund (S234602004-1 to Q.P.). **Author contributions:** Writing—original draft: Q.L., Y.W., and Q.P. Conceptualization: Q.L., K.Z., and Q.P. Writing—review and editing: L.D., J.Q., K.Z., W.S.S.G., Y.W., and Q.P. Methodology: Q.L., H.L., J.Q., and Q.P. Formal analysis: Q.L., J.L., L.G., Y.Z., Y.C., J.Q., and W.S.S.G. Investigation: Q.L., J.L., L.G., Y.Z., Y.C., H.C., and W.S.S.G. Resources: Q.L., J.Q., and Q.P. Visualization: Q.L. and Q.P. Supervision: Y.W. and Q.P. Data curation: Q.P. Validation: Q.L., J.L., L.G, Y.Z., Y.C., H.C., and Y.W. Funding acquisition: Q.L. and Q.P. Project administration: J.Q., Y.W., and Q.P. **Competing interests:** Q.P. has filed a patent application (202310605423.5, substantive examination) to China National Intellectual Property Administration for SMIS technology through the Shenzhen Bay Laboratory on 25 May 2023. Q.L., J.Q., J.L., and Y.C. are co-inventors on the patent. The other authors declare that they have no competing interests. **Data and materials availability:** All data needed to evaluate the conclusions in the paper are present in the paper and/or the Supplementary Materials. Sequencing data were deposited in NCBI's Gene Expression Omnibus (GEO) under accession number GSE273366.

Submitted 2 April 2024
Accepted 16 October 2024
Published 15 November 2024
10.1126/sciadv.adp5689